Department of
Industry and Resources

RECORD
2007/16

MAGNETOTELLURIC INVESTIGATION INTO THE ELECTRICAL STRUCTURE OF THE CAPRICORN OROGEN, WESTERN AUSTRALIA

by K Selway

Geological Survey of Western Australia

GEOLOGICAL SURVEY OF WESTERN AUSTRALIA

Record 2007/16

MAGNETOTELLURIC INVESTIGATION INTO THE ELECTRICAL STRUCTURE OF THE CAPRICORN OROGEN, WESTERN AUSTRALIA

by
K Selway[1]

[1] Continental Evolution Research Group, Geology and Geophysics, University of Adelaide, Adelaide, SA 5005

Perth 2008

MINISTER FOR ENERGY; RESOURCES; INDUSTRY AND ENTERPRISE
Hon. Francis Logan MLA

DIRECTOR GENERAL, DEPARTMENT OF INDUSTRY AND RESOURCES
Jim Limerick

EXECUTIVE DIRECTOR, GEOLOGICAL SURVEY OF WESTERN AUSTRALIA
Tim Griffin

REFERENCE
The recommended reference for this publication is:
Selway, K, 2008, Magnetotelluric investigation into the electrical structure of the Capricorn Orogen, Western Australia: Geological Survey of Western Australia, Record 2007/16, 39p.

National Library of Australia Card Number and ISBN 978-1-74168-118-5 (PDF)

Grid references in this publication refer to the Geocentric Datum of Australia 1994 (GDA94). Locations mentioned in the text are referenced using Map Grid Australia (MGA) coordinates, Zone 50. All locations are quoted to at least the nearest 100 m.

Cover image modified from Landsat data, courtesy of ACRES

Published 2008 by Geological Survey of Western Australia
This Record is published in digital format (PDF), as part of a digital dataset on CD, and is available online at www.doir.wa.gov.au/GSWA/publications. Laser-printed copies can be ordered from the Information Centre for the cost of printing and binding.

Further details of geological publications and maps produced by the Geological Survey of Western Australia are available from:
Information Centre
Department of Industry and Resources
100 Plain Street
EAST PERTH, WESTERN AUSTRALIA 6004
Telephone: +61 8 9222 3459 Facsimile: +61 8 9222 3444
www.doir.wa.gov.au/GSWA/publications

Contents

Figures

Table

Magnetotelluric investigation into the electrical structure of the Capricorn Orogen, Western Australia

by

K Selway[1]

Introduction

This Record describes a collaborative project between the Geological Survey of Western Australia and the University of Adelaide carried out from August 2006 to March 2007. The project involved the collection of approximately 300 line kilometres of magnetotelluric (MT) data in the northern Yilgarn Craton, Gascoyne Complex, and Edmund and Collier Basins in Western Australia and the subsequent processing, modelling and interpretation of those data. The aim of the project was to develop our understanding of the geological history of the Gascoyne region through obtaining information about its 3-dimensional structure from the MT data. The main results of this project are that:

1. Electrically, the margin between the Glenburgh Terrane and the Yilgarn Craton appears to dip south with crust of the Glenburgh Terrane wedged beneath the northern Yilgarn Craton;
2. There is no electrical distinction between the Glenburgh Terrane and the northern Gascoyne Complex; and
3. The main boundary between the Gascoyne Complex and the Pilbara Craton appears to correlate most closely with the Talga Fault.

This Record is presented in seven sections as follows:

1. Introduction;
2. Geological background, describing the current understanding of the region from geological and geophysical data as well as the rationale for carrying out MT in this region;
3. MT method, describing the theory behind the method;
4. Data collection, describing the process of data collection, instrumentation, survey layout, and rationale;
5. Data processing, describing the methods used to process the data and the results of this processing, particularly in terms of dimensionality and correlations with geological regions;
6. Modelling, describing the results of running 2D inversions and 3D forward models of the MT data; and
7. Synthesis, summarizing the project and results.

[1] Continental Evolution Research Group, Geology and Geophysics, University of Adelaide, Adelaide, SA 5005

Geological background

Overview

The Capricorn Orogen in central-west Western Australia contains granitic and metasedimentary rocks of the Gascoyne Complex and the deformed margins of the Archean Pilbara and Yilgarn Cratons as well as numerous deformed basins (Fig. 1; Cawood and Tyler, 2004). It records the juxtaposition of the Archean Yilgarn and Pilbara Cratons and the latest Archean to Paleoproterozoic Gascoyne Complex. The earliest interpretations of the Capricorn Orogen were of a geosyncline that formed in an ensialic setting, with no evidence found for any plate tectonic processes (Gee, 1979). However, Tyler and Thorne (1990) showed that the Pilbara and Yilgarn Cratons have different geological histories and that the Capricorn Orogeny therefore reflects the collision of two previously unrelated crustal volumes (Myers, 1993). Models based on this interpretation propose that a long-lived subduction-related arc existed in the Gascoyne Complex leading up to the Capricorn Orogeny (e.g. Krapez, 1999; Tyler and Thorne, 1990).

More recently, this interpretation has been refined through the implementation of routine SHRIMP U–Pb geochronology. These data have shown that the Capricorn Orogen actually underwent numerous individual tectonothermal events, most importantly the c. 2200 Ma Ophthalmian Orogeny, the 2005–1950 Ma Glenburgh Orogeny, the 1830–1780 Ma Capricorn Orogeny and the 1680–1620 Ma Mangaroon Orogeny (Cawood and Tyler, 2004; Kinny et al., 2004; Occhipinti et al., 2001; Sheppard et al., 2005). Furthermore, they have shown that the southern Gascoyne Complex, named the Glenburgh Terrane, is allochthonous to both the Yilgarn and Pilbara Cratons and collided with the Yilgarn Craton during the Glenburgh Orogeny (Occhipinti et al., 2004;

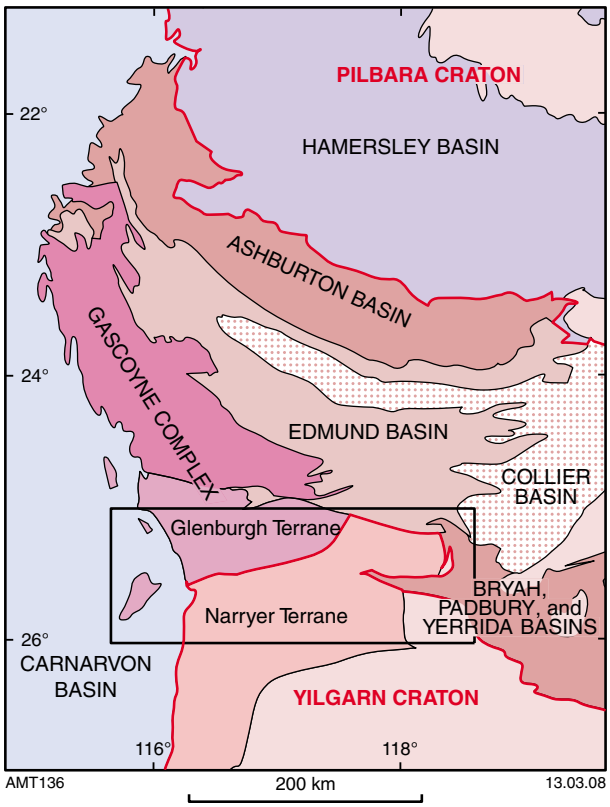

Figure 1. Overview map of the main geological regions surrounding the survey location, simplified from Cawood and Tyler (2004). The black box shows the location of the more detailed map in Figure 2

Sheppard et al., 2004). The Capricorn Orogeny is therefore not a simple, long-lived collisional event between the Pilbara and Yilgarn Cratons.

Lithotectonic elements

Yilgarn Craton — Narryer Terrane

The Narryer Terrane forms the northwestern part of the Yilgarn Craton. It consists of early Archean granitic gneisses which contain lenses and fragments of anorthosite and mafic to ultramafic rocks, and metasedimentary and metavolcanic rocks. Some of the metasedimentary rocks contain zircon dated at up to 4400 Ma. All of these rocks were intruded by late Archean granite and gabbro sheets (Cawood and Tyler, 2004; Occhipinti et al., 2001). The fault-bounded Yarlarweelor Gneiss Complex lies in the northern Narryer Terrane and is separated from the Glenburgh Terrane of the Gascoyne Complex to the north by the Errabiddy Shear Zone (Fig. 2). It was intruded by biotite monzogranite of the 1965–1945 Ma Bertibubba Supersuite and then deformed, metamorphosed, and intruded by granites during the 1830–1780 Ma Capricorn Orogeny (Kinny et al., 2004; Sheppard et al., 2003).

Figure 2. (below) Map of the lithological units in the Glenburgh Terrane and Narryer Terrane referred to in the text, simplified from Sheppard et al. (2003)

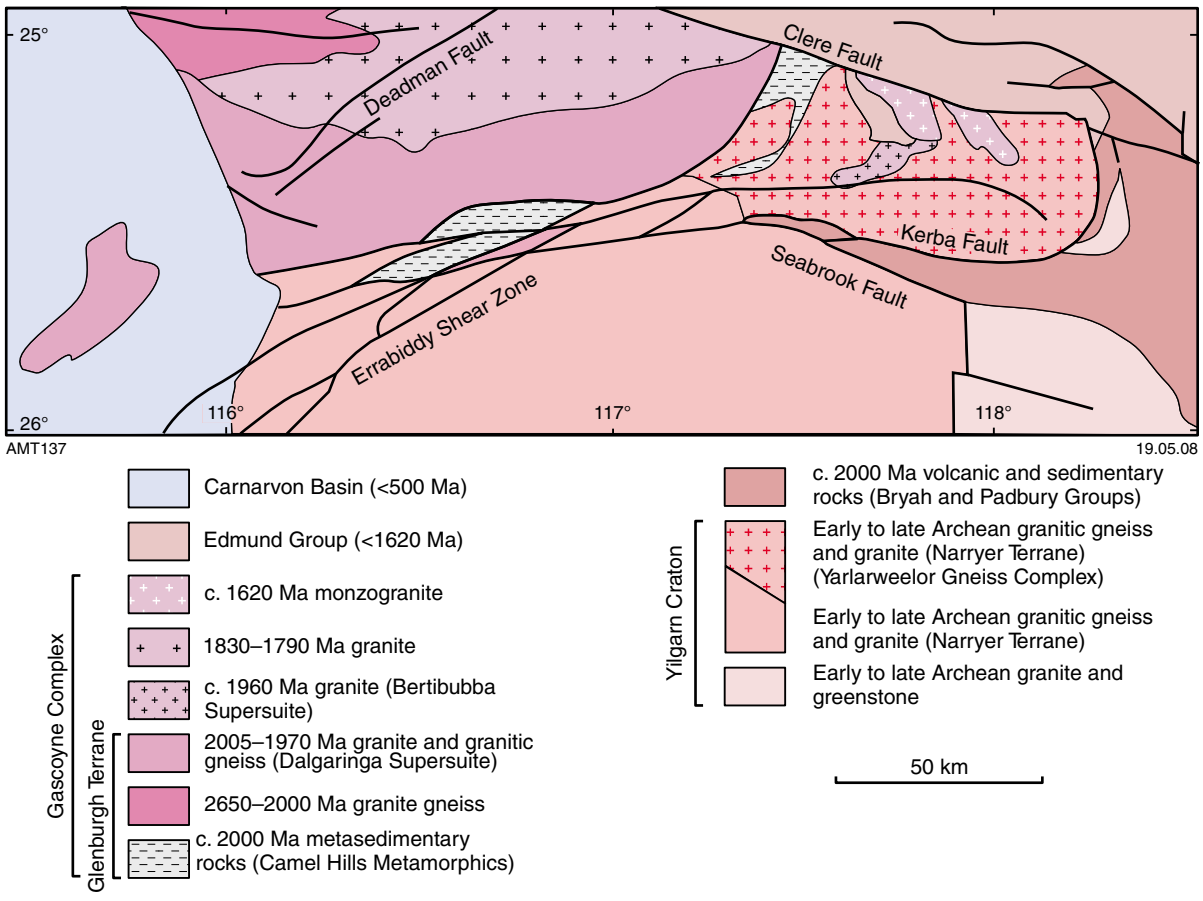

Errabiddy Shear Zone

The Errabiddy Shear Zone (Fig. 2) separates the Yilgarn Craton to the south from the Gascoyne Complex to the north. It is steeply dipping at the surface, has a strike length of 200 km and is up to 20 km wide (Occhipinti et al., 2001). It contains components of the Narryer Terrane, including fault-bounded slivers of the Yarlarweelor Gneiss Complex and intrusions of the Bertibubba Supersuite. It also contains the Camel Hills Metamorphics which consists of calc-silicate gneiss, pelitic schist, and gneiss that are confined to the shear zone. Detrital zircon analyses suggest that the latest Archean to Paleoproterozoic parts of the Glenburgh Terrane are a possible source of sediment for the pelitic schists, whereas the Yilgarn is a more likely source for the sedimentary protolith of the calc-silicate gneisses (Occhipinti et al., 2001; Occhipinti et al., 2004). Kinematic data suggest that movement on shear surfaces was both strike-slip and dip-slip (Reddy and Occhipinti, 2004). Zircon dating shows that deformation, with associated metamorphism up to the amphibolite facies, occurred during the Glenburgh Orogeny between 1975 and 1950 Ma with further deformation at greenschist facies during the Capricorn Orogeny (Occhipinti et al., 2004).

Glenburgh Terrane

The Glenburgh Terrane forms the southern Gascoyne Complex and comprises the Halfway Gneiss, the Dalgaringa Supersuite, and the Moogie Metamorphics. The Halfway Gneiss consists of late Archean (2650–2450 Ma) granites interleaved with younger 2005–1970 Ma calc-alkaline granites of the Dalgaringa Supersuite (Cawood and Tyler, 2004; Occhipinti et al., 2001). The Archean component of the Halfway Gneiss is younger than any granites dated on the northwest Yilgarn Craton and may form basement to the Glenburgh Terrane (Sheppard et al., 2004). The Dalgaringa Supersuite was deformed and metamorphosed during the Glenburgh Orogeny, which was followed by intrusion of granites of the 1965–1945 Ma Bertibubba Supersuite into both the Glenburgh and Narryer terranes. The Dalgaringa Supersuite has been interpreted to be an Andean-type batholith that formed in a subduction setting on latest Archean crust of the Glenburgh Terrane before collision of the Glenburgh and Narryer Terranes during the Glenburgh Orogeny (Sheppard et al., 2004). The Moogie Metamorphics consist of supracrustal rocks including mafic schist and gneiss, pelitic schist, calc-silicate gneiss, and dolomitic marble (Occhipinti et al., 2004).

Bertibubba Supersuite

Granites of the 1965–1945 Ma Bertibubba Supersuite intruded into the Glenburgh and Narryer terranes following the Glenburgh Orogeny. This is the first event common to both terranes and therefore provides a lower age limit for their juxtaposition (Sheppard et al., 2004). Neodymium isotopic data suggest that the source for the Bertibubba Supersuite is the Dalgaringa Supersuite with a minor Archean component, suggesting that crust of the Glenburgh Terrane may be wedged beneath the Narryer Terrane (Sheppard et al., 2004).

Northern Gascoyne Complex

The northern Gascoyne Complex consists of extensive medium- to high-grade metamorphic rocks intruded by granitic plutons. The metamorphic rocks include pelitic and psammitic schist, calc-silicate schist, amphibolite, and quartzite of the Morrisey Metamorphics (Cawood and Tyler, 2004). These are intruded by granites of the 1810–1780 Ma Minnie Creek batholith (Williams, 1986). The c. 1680 Ma Pooranoo Metamorphics lie unconformably on top of the Minnie Creek batholith. After being deformed and metamorphosed during the Mangaroon Orogeny, the Pooranoo Metamorphics were then intruded by granites of the 1680–1620 Ma Durlacher Supersuite. Tyler and Thorne (1990) interpreted the Minnie Creek batholith as the pluton that stitched the suture between the Yilgarn and Pilbara Cratons during the Capricorn Orogeny. More recent interpretations suggest that it may have formed during the collision of the combined Glenburgh Terrane and Yilgarn Craton with the Pilbara Craton (e.g. Hackney, 2004) or alternatively, if the Gascoyne Complex had accreted to the Pilbara Craton before accreting to the Yilgarn Craton, the Minnie Creek batholith may have been simply been formed during intracratonic deformation (Sheppard et al., 2001). No evidence has been found in the northern Gascoyne Complex of rocks that correlate with the Dalgaringa Supersuite or Halfway Gneiss of the Glenburgh Terrane, leaving the relationship between the northern Gascoyne Complex and the Glenburgh Terrane unknown (Cawood and Tyler, 2004).

Bangemall Supergroup

The Mesoproterozoic Bangemall Supergroup is divided into the lower 1620–1465 Ma Edmund Group and the upper 1400–1070 Ma Collier Group (Martin and Thorne, 2004). Depositional ages of the Bangemall Supergoup are poorly defined and are largely constrained through dating of two generations of dolerite sills that intrude the basins at c. 1465 Ma and 1070 Ma. Sedimentation of the Bangemall Supergroup was strongly influenced by primary structural controls that follow the trends of major structures in the underlying Ashburton Fold Belt and Gascoyne Complex, notably the Talga Fault and the Wanna Syncline (Martin and Thorne, 2004). The Supergroup was deformed during the Edmundian Orogeny, some time between 1070 and 750 Ma, producing upright open folds with localized thrusting and reactivation of syndepositional faults (Martin and Thorne, 2004).

Ashburton Basin

The Ashburton Basin contains variably deformed, low-grade metasedimentary and metavolcanic rocks of the upper and lower Wyloo Group to a thickness of approximately 12 km (Thorne, 1990). Detrital zircon populations from the lower Wyloo Group shows a complex late Archean to early Paleoproterozoic source while detrital zircon from the upper Wyloo Group suggest a provenance

consistent with derivation from the Gascoyne Complex and Narryer Terrane (Sircombe, 2002).

Hamersley Basin

The Hamersley Basin forms part of the Archean Pilbara Craton. It sits unconformably on early–middle Archean granite–greenstones of the Pilbara Craton and is in turn unconformably overlain by the Ashburton Basin (Cawood and Tyler, 2004). Three groups are recognized within the Hamersley Basin. The lowermost Fortescue Group, comprises felsic, mafic, and ultramafic metavolcanic rocks and metasedimentary rocks. The middle Hamersley Group is dominated by banded iron-formation, shale, carbonate sedimentary rocks, and felsic igneous rocks, whereas the upper Turee Creek Group consists mostly of fine- to coarse-grained clastic metasedimentary rocks (Thorne and Trendall, 2001). Hamersley Basin rocks are intruded by mafic to ultramafic sills and the entire succession was deformed during the Ophthalmian and Capricorn Orogenies (Tyler and Thorne, 1990).

Event chronology

Ophthalmian Orogeny

The Ophthalmian Orogeny affected the Ashburton and Hamersley Basins and formed the Ophthalmian Fold Belt, and is characterized by west to northwest trending, north-vergent folds and thrusts (Tyler and Thorne, 1990). It has a SHRIMP U–Pb monazite age of 2215–2145 Ma (Rasmussen et al., 2005). The driving forces behind the Ophthalmian Orogeny are unknown, although it has been suggested that it was related to the collision of the Gascoyne Complex with the Pilbara Craton (Occhipinti et al., 2004).

Glenburgh Orogeny

The Glenburgh Orogeny affected the Glenburgh Terrane and the northern margin of the Yilgarn Craton. It consists of two stages of deformation. The first affected only the Glenburgh Terrane and deformed the earliest granites of the Dalgaringa Supersuite, dated at c. 2000 Ma (Occhipinti et al., 2004). The second stage extends into the Errabiddy Shear Zone and the Yarlarweelor Gneiss Complex in the Narryer Terrane and produced metamorphism up to amphibolite facies. The age of deformation is constrained by the fact that it affects the c. 1975 Ma Nardoo Granite but predates intrusion of the 1965–1945 Ma Bertibubba Supersuite (Cawood and Tyler, 2004). The Glenburgh Orogeny has been interpreted to reflect the collision between the Glenburgh Terrane and the Yilgarn Craton (e.g. Occhipinti et al., 2004; Sheppard et al., 2004).

Capricorn Orogeny

The Capricorn Orogeny is a wide-ranging event that affected the lithological units between the southern margin of the Pilbara Craton and the northern margin of the Yilgarn Craton and therefore provides a minimum age limit for their juxtaposition. The orogeny was associated with the emplacement of numerous granites of the 1830–1780 Ma Moorarie Supersuite, which includes the Minnie Creek batholith (Occhipinti et al., 1998; Occhipinti et al., 2001; Occhipinti et al., 2004). It was also associated with pervasive deformation and metamorphism throughout most of the Gascoyne Complex and sedimentation into basins in the Gascoyne Complex and Yilgarn Craton including the Ashburton, Blair, and Earaheedy Basins (Halilovic et al., 2004; Pirajno et al., 2004). Data from these events has constrained the Capricorn Orogeny to 1830–1780 Ma. Early interpretations suggested that the Capricorn Orogeny was related to the collision of the Pilbara and Yilgarn Cratons (Myers, 1993; Tyler and Thorne, 1990). However, more recent data have shown that the Glenburgh Terrane had already accreted onto the Yilgarn Craton during the Glenburgh Orogeny (Occhipinti et al., 2004; Sheppard et al., 2004). The Capricorn Orogeny may reflect collision of the Pilbara Craton with the combined Yilgarn Craton and Gascoyne Complex, but granites in the Glenburgh Terrane associated with the Capricorn Orogeny do not show any evidence for the introduction of mantle derived material, suggesting that it may instead reflect intracratonic reworking (Sheppard et al., 2001).

Mangaroon Orogeny

The Mangaroon Orogeny is a recently recognized event that affected much of the Gascoyne Complex (Sheppard et al., 2005). It is associated with deformation of sediments that were deposited after 1680 ± 13 Ma, and emplacement of granites with crystallization ages of 1680–1620 Ma. It is interpreted to be an intracratonic event due to the lack of associated arc magmatism, combined with the low-P/high-T nature of metamorphism and abundant S-type granites (Sheppard et al., 2005). Many of the features that have been identified as part of the Mangaroon Orogeny were previously interpreted to be associated with the Capricorn Orogeny, leading Sheppard et al. (2005) to suggest that undated tectonothermal events in other tectonic units currently thought to be related to the Capricorn Orogeny may also instead be associated with the Mangaroon Orogeny.

Edmundian Orogeny

The intracratonic Edmundian Orogeny deformed rocks of the Gascoyne Complex and the Edmund and Collier Basins. Its age is constrained by pre- and post-deformational mafic intrusions with ages of 1070 Ma and 750 Ma (Martin and Thorne, 2004; Wingate and Giddings, 2000). The Edmundian Orogeny is interpreted to be related to the rifting of Australia and Antarctica from Laurentia during the breakup of Rodinia (Cawood and Tyler, 2004; Powell et al., 1994).

Geophysics

Gravity

Hackney (2004) computed a gravity model of the Capricorn Orogen. The main features in this model are the Yerrida, Collier, Edmund, and Ashburton Basins and the

Hamersley Province within the uppermost 10 km of the crust. The middle and lower crust is relatively continuous across the model, as is common in gravity data, with little to no distinction between the Yilgarn Craton, Gascoyne Complex and Pilbara Craton. The authors interpret the model to represent the crust of the Pilbara Craton extending beneath that of the Yilgarn Craton at depth with a south-dipping margin, with the allochthonous crust of the Glenburgh Terrane sitting above the margin between the cratons. However, since the gravity data has little sensitivity to structures at such depths, this interpretation is somewhat speculative and appears strongly influenced by previous tectonic models (e.g. Myers, 1993; Tyler and Thorne; 1990), rather than being required by the data.

Seismic refraction

Drummond (1981) describes the results of several seismic refraction surveys in the Pilbara Craton, Ashburton Trough, Bangemall Supergroup, Gascoyne Complex, and northern Yilgarn Craton. The resulting models show significant differences in crustal thickness across the region. The crust of the Pilbara Craton was modelled to be 28 km thick in the north and 30–33 km thick in the south. There is a sharp increase in crustal thickness to approximately 40 km thick at the northern margin of the Ashburton Basin, interpreted to mark the boundary of the Capricorn Orogen. The Yilgarn Craton crust was modelled to be more than 50 km thick. This thick crust appears to begin just south of the Errabiddy Shear Zone, and the shallower crust of the northern Yilgarn Craton is interpreted to have been reworked during the Capricorn Orogeny.

Reading et al. (2007) describe new results for seismic receiver functions across the region. The resulting depths to Moho are similar to the results described above for the Pilbara Craton (32 km) and the Capricorn Orogen (44 km), but the Moho depth in the Yilgarn Craton was found to vary between 34 km in the north-western Murchison terrane to 42 km in the Eastern Goldfields terrane, compared to more than 50 km as suggested by Drummond (1981). The authors note that these results imply that the seismic structure of the surveyed Archean terranes has been preserved since before the assembly of the West Australian Craton.

Main areas of investigation with MT

Magnetotellurics (MT) is a passive electromagnetic geophysical technique that images the electrical resistivity of the Earth. Depth resolutions into the upper mantle are easily achievable. MT surveys have been carried out in many regions of geological interest over the Earth, most notably in North America as part of the LITHOPROBE program (Ferguson et al., 2005a,b; Garcia and Jones, 2005; Jones and Gough, 1995), in Tibet as part of the INDEPTH program (Spratt et al., 2005; Unsworth et al., 2005), in New Zealand (Wannamaker et al., 2002), and recently in central and southern Australia (Heinson et al., 2006; Selway et al., 2006a).

There are three main causes for enhanced electrical conductivity within the earth: fluids, sulphides and graphite. In fluids, electricity conducts through movement of ions, so the fluids need to be free and sufficiently interconnected that pathways exist for the ions to move along. In the Earth, this is generally reflected as melts (e.g. Wannamaker et al., 1989) or as brine in porous sedimentary rocks (e.g. Tournerie and Chouteau, 2005). Conduction in sulphides is through movement of electrons and again requires an interconnected pathway. Therefore, although sulphides are often the cause of enhanced conductivity in discrete mineralized bodies (e.g. Livelybrooks et al., 1996), they can rarely explain regional scale conductivity anomalies (e.g. Jones et al., 2005a). Instead, enhanced conductivity on a regional scale is generally interpreted to be caused by interconnected graphite films (Glover, 1996 and references therein). Graphite bodies or even flakes of graphite are not standard constituents of crustal rocks and would not provide the interconnected pathways necessary to explain observed enhanced conductivities. However, Auger spectrometry analysis of many samples representative of Precambrian crust has identified graphite films on many grain boundaries (Frost et al., 1989; Hauk et al., 1997; Mareschal et al., 1992; Mathez et al., 1995). These films, although as thin as 10 Angstroms, are interconnected and can enhance the conductivity of a crystalline rock to that observed in MT studies of the crust and mantle (Duba et al., 1994; Duba et al., 1988; Glover and Vine, 1992; Glover and Vine, 1995; Mathez et al., 1995). With these causes for enhanced conductivity in mind, results from MT surveys have been interpreted to represent geological features such as fluid exsolution from a subducting slab (e.g. Soyer and Unsworth, 2006; Wannamaker et al., 1989), fossil subduction zones (e.g. Jones, 1993; Jones et al., 2005b; Selway et al., 2006b), contrasting bulk lithologies between different crustal blocks (e.g. Jones et al., 2002; Selway et al., 2006a), sedimentary basins (e.g. Tournerie and Chouteau, 2005), and major faults and shear zones (e.g. Garcia and ones, 2005; Jödicke et al., 2004; Unsworth et al., 1997).

An approximately 300 km long MT survey was carried out extending from the Yilgarn Craton in the south, over the Gascoyne Complex and into the Bangemall Supergroup with the aim of developing the geological understanding of the region as follows:

1. **Suturing of the Glenburgh Terrane and the Yilgarn Craton along the Errabiddy Shear Zone**: Surface geological evidence shows that the Glenburgh Terrane is exotic to the Yilgarn Craton and that the two collided along a margin now defined by the Errabiddy Shear Zone. The Bertibubba Supersuite, which intruded both the Glenburgh Terrane and the Narryer Terrane of the northern Yilgarn Craton immediately following this collision, shows isotopic evidence of being sourced from the Dalgaringa Supersuite of the Glenburgh Terrane. This suggests that the Glenburgh Terrane may have been wedged beneath the northern margin of the Yilgarn Craton during collision. The first aim of the MT profile was to image the crust of the Glenburgh Terrane and the Narryer Terrane at depth, determining whether they have contrasting electric characteristics

and also determining the dip of the boundary between the two terranes.

2. **Relationship between the Glenburgh Terrane and the northern Gascoyne Complex**: The Glenburgh Terrane in the southern Gascoyne Complex is allochthonous to the Yilgarn and Pilbara Cratons. Correlatives of the basement rocks of the Glenburgh Terrane have not been identified in the northern Gascoyne Complex, where outcropping geology is restricted to younger igneous and metamorphic rocks. The nature of the basement to these packages is unknown. The second aim of the MT profile was to investigate the electrical nature of the crust of the whole Gascoyne Complex and specifically to determine whether the basement to the northern Gascoyne Complex appears to correlate to the Glenburgh Terrane or to a different unit such as the Pilbara Craton.

3. **Location and nature of the boundary between the Gascoyne Complex and the Pilbara Craton**: In outcrop, the boundary between the Gascoyne Complex and the Pilbara Craton is obscured by younger sediments of the Bangemall Supergroup. Deposition of Bangemall Supergroup sediments was controlled by primary structures defined by major faults in the underlying basement, which may represent structures related to the suturing of the Gascoyne Complex and the Pilbara Craton. Alternatively, as noted above, crust of the Pilbara Craton could form basement to the northern Gascoyne Complex, with the major suture being between the northern Gascoyne Complex and Glenburgh Terrane. Since MT is able to image lithospheric structure beneath sedimentary basins, the third aim of the profile was to investigate whether a major electrical boundary exists between the Gascoyne Province and the Pilbara Craton, beneath the Bangemall Supergroup. A second aim was to image the effect of these major depositional structures on the Bangemall Supergroup itself.

MT theory

Magnetotellurics (MT; Cagniard, 1953; Simpson and Bahr, 2005; Swift, 1971; Telford et al., 1990; Tikhonov, 1950; reprinted as Tikhonov, 1986; Vozoff, 1991) is a passive sounding method that utilizes naturally occurring geomagnetic variations as a source for electromagnetic induction within the Earth. MT images electrical resistivity (or its inverse, conductivity) within the Earth and can resolve depths of tens of meters to several hundred kilometres.

Induction

A time changing magnetic field will induce a current in a conductive body, which will then generate associated electric and magnetic fields. The source field used in the MT method is the Earth's magnetic field (Cagniard, 1953), which is time-changing due to electrical storms at short periods (<1 s) and due to the interaction between the Earth's magnetosphere and ionosphere and solar wind at longer periods (>1 s). Electrical currents and electric fields are generated in conductive bodies within the Earth. Electromagnetism is described by Maxwell's equations. With the assumptions that at MT periods the displacement currents are negligible (Simpson and Bahr, 2005), Maxwell's equations are:

$$\nabla \times \mathbf{E} = -\frac{\partial \mathbf{B}}{\partial t} \tag{1}$$

$$\nabla \times \mathbf{B} = \mu_0 \sigma \mathbf{E} \tag{2}$$

$$\nabla \cdot \mathbf{B} = 0 \tag{3}$$

$$\nabla \cdot \mathbf{E} = \frac{\eta_f}{\varepsilon} \tag{4}$$

$$\mathbf{j} = \sigma \mathbf{E} \tag{5}$$

where $\mathbf{E}$ is the electric field intensity in V/m, **B** is the magnetic induction in T (**B**=μ**H**) where **H** is the magnetic field intensity in A/m), η_f is the electric charge density due to free charges in C/m^3, ε is the electric permitivity, **j** is the electric current density due to electric displacement in A/m^2 and σ is conductivity in Sm^{-1}. Equation (1) is a mathematical statement of Faraday's law that a time varying magnetic field generates an electric field with an induced emf proportional to the rate of change of magnetic flux. Equation (2) is a mathematical statement of Ampere's law that a magnetic field is generated by current flow. Equation (5) is a statement of Ohm's law that current density is directly proportional to the electric field strength.

A diffusion equation can be derived by taking the curl of Equation (1) or (2), which will provide information about the conductivity structure of the Earth. The diffusion equation is

$$\nabla^2 \mathbf{E} = \mu_0 \sigma \frac{\partial \mathbf{E}}{\partial t} \tag{6}$$

and

$$\nabla^2 \mathbf{B} = \mu_0 \sigma \frac{\partial \mathbf{B}}{\partial t} \tag{7}$$

Assuming a plane wave (Cagniard, 1953; Madden and Nelson, 1964, reprinted 1986) with surface amplitude of E_0 and a time dependence of $e^{i\omega t}$, Equations (6) and (7) become

$$\nabla^2 \mathbf{E} = i\omega\mu_0\sigma\mathbf{E} \tag{8}$$

and

$$\nabla^2 \mathbf{B} = i\omega\mu_0\sigma\mathbf{B} \tag{9}$$

Electromagnetic fields therefore propagate diffusively, with the result that MT measurements are volume soundings, yielding a volumetric average of the conductivity of the region sampled.

An important value in MT is the complex impedance Z (Cantwell, 1960), which relates the incident magnetic and

induced electric fields in the subsurface and is determined by the relation

$$\begin{vmatrix} E_x \\ E_y \\ E_z \end{vmatrix} = \begin{vmatrix} Z_{xx} & Z_{xy} & Z_{xz} \\ Z_{yx} & Z_{yy} & Z_{yz} \\ Z_{zx} & Z_{zy} & Z_{zz} \end{vmatrix} \begin{vmatrix} H_x \\ H_y \\ H_z \end{vmatrix} \quad (10)$$

If only the horizontal field components are considered and the assumptions made that H_z=0 for a plane wave source propagating in the z direction and that J_z=0 at the surface as current can not flow into the air, the tensor reduces to

$$\begin{vmatrix} E_x \\ E_y \end{vmatrix} = \begin{vmatrix} Z_{xx} & Z_{xy} \\ Z_{yx} & Z_{yy} \end{vmatrix} \begin{vmatrix} H_x \\ H_y \end{vmatrix} \quad (11)$$

Apparent resistivity and phase

Since MT is a volume sounding method, the impedance tensor measured at any period will be the volumetric average of impedance tensors at that period and all periods less than it. Therefore, unless the subsurface is a uniform half-space, resistivity at a point cannot be directly calculated. Instead, the apparent resistivity parameter is calculated. Apparent resistivity, ρ_a, is defined as the skin-depth (see Section 3.4) weighted average resistivity of an equivalent uniform half-space (Telford et al., 1990) and is calculated from the impedance tensor through the relation:

$$\rho_a = \frac{1}{\mu\omega}[Z]^2 \quad (12)$$

Since the impedance tensor is complex it also contains information on the phase Φ. Physically, this parameter reflects the fact that there is a phase lag between the inducing magnetic and induced electric fields and is calculated by the relation:

$$\Phi = arctan(Z) \quad (13)$$

Apparent resistivity and phase are linked by the Kramers-Kroenig relationship (Wiedelt, 1972) which shows that, in the absence of distortion, the phase can be calculated from the apparent resistivity:

$$\phi(\omega) = \frac{\pi}{4} - \frac{\omega}{\pi}\int_0^\infty \log\frac{\rho_a(x)}{\rho_0}\,\frac{dx}{x^2-\omega^2} \quad (14)$$

Dimensionality

The behaviour of the fields and impedance tensor varies depending on the electrical dimensionality of the Earth. The simplest Earth is a homogenous half-space. A one-dimensional (1D) earth is a horizontally layered half-space where conductivity changes only in the vertical (z) direction but in neither of the horizontal (x or y) directions (Fig. 3a). Conductivity of a two-dimensional (2D) Earth changes both vertically and in one direction horizontally (Fig. 3b) while conductivity of a three-dimensional (3D) Earth changes in the vertical and both horizontal directions (Fig. 3c).

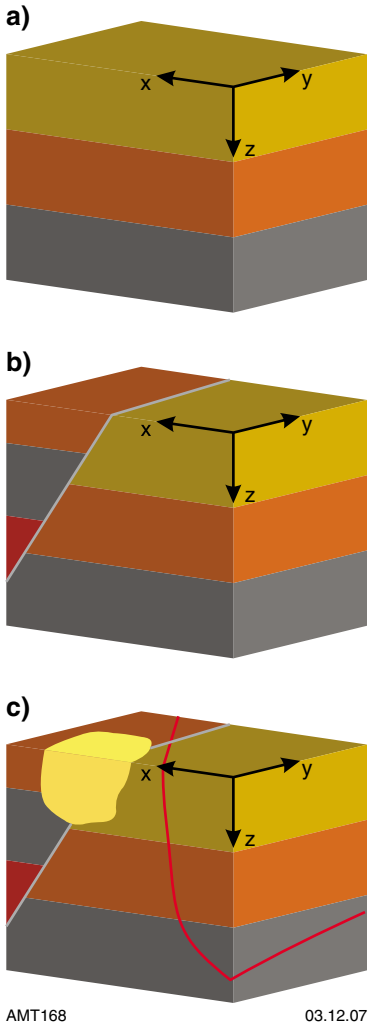

Figure 3. **a) the resistivity of a 1D earth changes only in the vertical direction; b) the resistivity of a 2D earth changes in the vertical direction and one horizontal direction, with a constant and infinite strike; c) the resistivity of a 3D earth changes in all three directions**

The impedance tensor (Equation 11) contains useful information about the dimensionality of the subsurface. In a 1D situation, electric fields are only induced orthogonal to the inducing magnetic fields, so Z_{xx} and Z_{yy} are both zero. Since there are no lateral conductivity gradients, a magnetic field will induce an electric field of the same strength in any direction, so $|Z_{xy}| = |Z_{yx}|$ but these values will have different signs, such that, whatever direction the x and y axes are in,

$$\begin{vmatrix} E_x \\ E_y \end{vmatrix} = \begin{vmatrix} 0 & Z_{xy} \\ -Z_{xy} & 0 \end{vmatrix} \begin{vmatrix} H_x \\ H_y \end{vmatrix} \quad (15)$$

In a 2D situation with the x and y axes orientated randomly, $Z_{xx}$and Z_{yy} will be equal in magnitude but opposite in sign while Z_{xy} and Z_{yx} will differ, such that

$$\begin{vmatrix} E_x \\ E_y \end{vmatrix} = \begin{vmatrix} Z_{xx} & Z_{xy} \\ Z_{yx} & -Z_{xx} \end{vmatrix} \begin{vmatrix} H_x \\ H_y \end{vmatrix} \quad (16)$$

However when the axes are oriented parallel and perpendicular to electromagnetic strike, Z_{xx} and Z_{yy} become zero, while Z_{xy} and Z_{yx} remain different

$$\begin{vmatrix} E_x \\ E_y \end{vmatrix} = \begin{vmatrix} 0 & Z_{xy} \\ Z_{yx} & 0 \end{vmatrix} \begin{vmatrix} H_x \\ H_y \end{vmatrix} \quad (17)$$

In this situation, the MT tensor decomposes into two independent modes: the transverse electric (TE) mode (also referred to as the E polarization or E-pol mode), where the electric field is measured parallel to strike; and the transverse magnetic (TM) mode (also referred to as the B polarization or B-pol mode) where the magnetic field is measured parallel to strike.

Taking x as the strike direction and y as the direction perpendicular to strike, for the TM mode Ampere's law reduces to

$$\frac{\partial B_x}{\partial y} = -\mu\sigma(y,z)E_z \quad (18)$$

and

$$\frac{\partial B_x}{\partial z} = -\mu\sigma(y,z)E_y \quad (19)$$

For the TE mode Faraday's law reduces to

$$\frac{\partial E_x}{\partial y} = i\omega B_z \quad (20)$$

and

$$\frac{\partial E_x}{\partial z} = i\omega B_y \quad (21)$$

The TE mode is therefore independent of E_y and E_z and is represented by the impedance Z_{xy}. The TM mode is independent of E_x and is represented by the impedance Z_{yx}.

This decomposition greatly simplifies MT data processing and modelling and most MT surveys are therefore carried out under an approximation of a 2D geoelectric environment.

At a vertical boundary with strike x between two media of different conductivities, the following boundary conditions must be obeyed (Swift, 1971)

- The component of B perpendicular to the interface (μH_y) is continuous.
- The component of H parallel to the interface (H_x) is continuous.
- The component of E parallel to the interface (E_x) is continuous.
- The current density J perpendicular to the interface (σE_y) is continuous.

The only discontinuous quantity is Ey, the electric field perpendicular to the interface. This must have a discontinuity at the interface since the conductivity across the boundary changes but the current density must remain continuous, and

$$E_y = \frac{J_y}{\sigma} \quad (22)$$

The TE mode will not be affected by this boundary as it is independent of E_y, but the TM mode will be affected.

Charge distributions build up in the region of the interface (Vozoff, 1991; Wannamaker et al., 1984). These charge distributions, often referred to as current gathering, produce electric fields in the –y and y directions. These secondary fields add vectorially to the inducing E_y field in each medium. On the more conductive side, the resultant electric field is

$$E_{res} = E_{y\,primary} - E_{y\,secondary} \quad (23)$$

Due to the inverse relationship between the electric field and the apparent conductivity in Equation (12), this decrease in the electric field will increase the apparent conductivity of the conductor.

Similarly, on the more resistive side of the fault, the resultant electric field is

$$E_{res} = E_{y\,primary} + E_{y\,secondary} \quad (24)$$

and the increase in the magnetic field makes the resistor look even more resistive. This effect allows for accurate delineation of boundaries in the TM mode and the under- and over-estimated resistivity values are corrected by most 2D modelling algorithms (Wannamaker et al., 1984).

Penetration depth

Long period signals penetrate deeper within the Earth than short period signals. The depth at which a signal has strength e^{-1} of its amplitude at the surface is considered to be the maximum depth that information can be gained from that signal and is referred to as the skin depth d, with equation (Simpson and Bahr, 2005)

$$d = \left(\frac{T}{\pi\mu\bar{\sigma}}\right)^{\frac{1}{2}} \quad (25)$$

where T is period, μ is magnetic permeability and $\bar{\sigma}$ is the average conductivity of the medium penetrated. In MT studies, μ can be approximated by the free space magnetic permeability $\mu_0 = 4\pi \times 10^{-7}\ Hm^{-1}$ which reduces Equation (25) to

$$d \approx 500\sqrt{T\rho_a} \quad (26)$$

Therefore a longer recording time of MT signal results in a larger depth penetration and resistivity information about greater depths within the Earth.

Induction arrows

Where lateral conductivity gradients exist, vertical magnetic fields (H_z) are induced by the horizontal magnetic fields as described by the relationship (Simpson and Bahr, 2005)

$$H_z(\omega) = \left(T_x(\omega)\ T_y(\omega)\right) \begin{pmatrix} \frac{B_x}{\mu_0} \\ \frac{B_y}{\mu_0} \end{pmatrix} \quad (27)$$

Induction arrows are vector representations of the complex ratio of the vertical to horizontal magnetic fields. In the Wiese convention (Wiese, 1962), real (in-phase) induction arrows point away from regions of high conductivity (or towards regions of high resistivity). However induction arrows are more commonly displayed in the Parkinson convention (Parkinson, 1959) in which they point towards regions of high conductivity, or away from regions of high resistivity. The length of induction arrows is dependent on the magnitude of the resistivity gradient.

In a simple 2D environment with a single resistivity boundary, induction arrows will point perpendicular to the boundary and in the Parkinson convention, towards the region of higher conductivity. However in more complex 2D environments, for instance where a region of high resistivity is bounded by two regions of high conductivity, the induction arrow pattern will be more complex and the magnitude of induction arrows in the central high conductivity region may be negligible even though significant conductivity gradients exist (Jones and Price, 1970).

Data collection

Survey plan

An MT survey was carried out in central-western Western Australia in September and October 2006. The survey location (Fig. 4) was designed to cross the Errabiddy Shear Zone, which marks the boundary between the Yilgarn Craton and the Gascoyne Complex; the boundary between the Glenburgh Terrane and the northern Gascoyne Complex (marked at the surface by the Chalba Fault); and the Wanna Syncline and Talga Fault which provided a fundamental control on sedimentation of the Bangemall Supergroup and may be related to the boundary between the Gascoyne Complex and the Pilbara Craton.

An early concern was that the Errabiddy Shear Zone, the Chalba Fault, and the Talga Fault have different strike directions at the surface. 2D MT surveys require a 2D subsurface, where geoelectric strike direction is constant along the profile and does not change significantly along

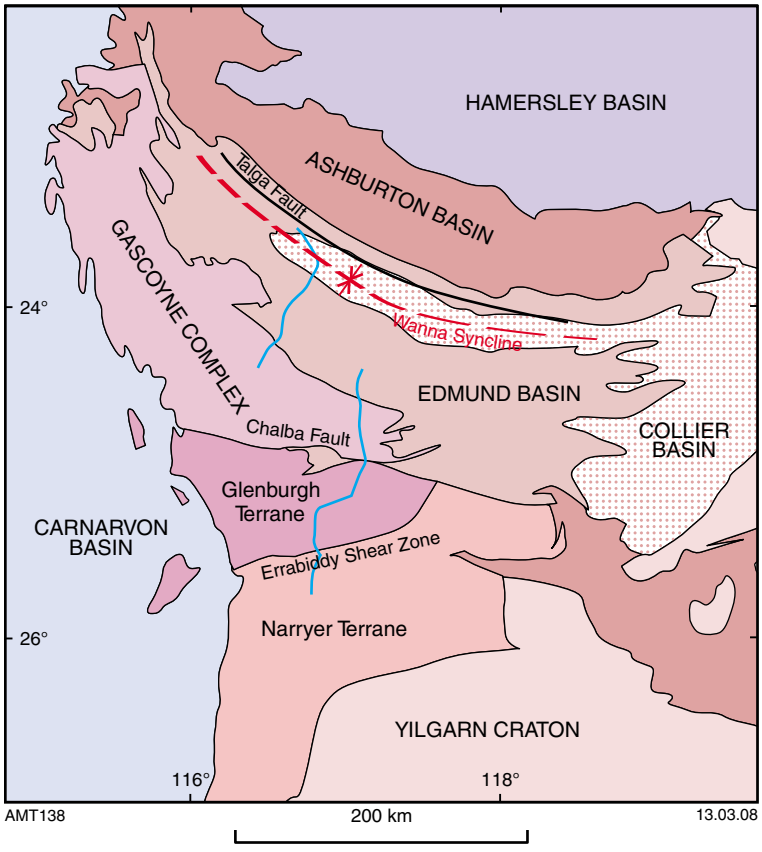

Figure 4. Geological map of the Gascoyne region with the location of the planned MT traverses shown in blue

its length. The location of the southern portion of the profile was chosen such that the profile would cross the Errabiddy Shear Zone and the Chalba Fault where they have similar strike directions, even though the strike directions of both faults change to the east of the profile. The southern profile was carried out along two roads which run approximately perpendicular to the strike of the major faults, with a 20 km east-west offset between them. There was no flexibility in choosing the location of the northern portion of the profile as only one accessible road extends into the area of interest across the Bangemall Supergroup. This road runs approximately perpendicular to the strike of the Talga Fault. The strike of the Talga Fault is approximately 50° different to the strike of the Errabiddy and Chalba Faults where they cross the southern profile. It is therefore possible that the southern and northern profiles will show different geoelectric strike directions, preventing a 2D model being made from the whole profile. In this eventuality, the survey design easily allows for separate 2D inversions of the southern and northern profiles, each with a different geoelectric strike direction. There is a 65 km, approximately east–west offset between the southern and northern profiles.

The total line length of the planned profiles was approximately 300 km. Station spacing was set at 5 km to allow for good resolution of crustal-scale features, even in the event of data collection failing at some stations. Recording time was set to at least three days per station to yield period ranges of ~10 s to ~3000 s, giving depth resolution to crustal to upper mantle depths in average lithosphere (Equation 26; Jones, 1999). At 5 km spacing along the planned profiles, with stations at the start and end of each section, the total number of stations is 55. Scheduling this with three days recording time, 10 instruments, and time to go to Carnarvon to restock fuel and food leads to an expected survey length of 21 days. From past experience it is prudent to schedule significantly more time into surveys than would be expected to allow for instrument breakdown, failure of data collection at stations and any number of unexpected logistical problems. Therefore four weeks of field time were allocated to the survey.

Equipment

Adelaide University has two generations of MT instruments. Both are five-component systems, which record the two horizontal components of the electric field and the two horizontal components and the vertical component of the magnetic field. Magnetic fields are measured using a Bartington three component fluxgate magnetometer which has sensitivity at frequencies lower than 1 Hz and a precision of ~10 pT. Noise levels are quoted as ~5 pT/√Hz at 1 Hz. Electric fields are measured using pairs of copper/copper sulphate porous pots separated by distances (d) of between 20 and 50 m. By measuring the voltages (V) at each electrode, the electric field (E) can be determined by the equation:

$$Ed = V \qquad (28)$$

Instruments are powered by gel cell batteries, which are housed with the logging electronics inside Pelican cases for protection. The magnetometers (Fig. 5) are housed in separate Pelican cases to prevent contamination by any electromagnetic noise being emitted by the electronics. Data are recorded onto CF cards in files that each contain one hour of data. Each hour of data is referred to as a block.

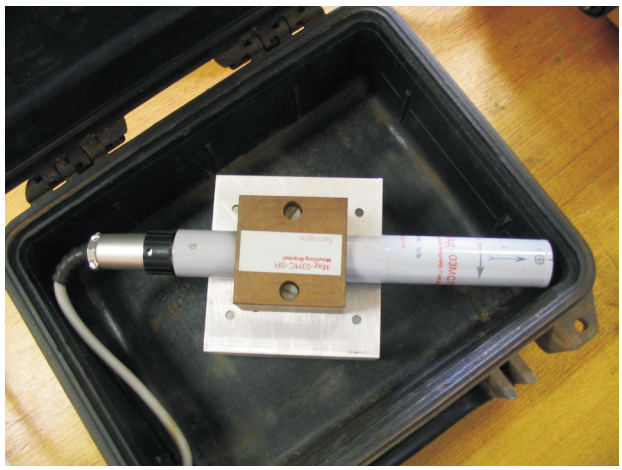

AMT139 06.11.07

Figure 5. Bartington three-component fluxgate magnetometer, housed in a Pelican case for protection

The five first-generation Adelaide University MT instruments have been in use since 2002–03. They run off 12V batteries that can power the instruments for three to four days when data are sampled at 10 Hz. In 2006 a second generation of instruments was built. These instruments are run off 6V batteries that can power the instruments for up to seven days. The analogue-to-digital converter board used in the first generation was updated to a new board that includes a GPS input. The GPS input not only automatically records the station location, it more importantly also ensures that data are recorded at exactly one second intervals. The first-generation instruments are timed by internal clocks that drift over the course of several days' recording, which can lead to difficulties in remote referencing. The inclusion of GPS timing eliminates this problem.

The first of the second generation of instruments was built in mid-2006 and used in two surveys conducted by other members of the University of Adelaide MT group prior to the Gascoyne survey. This prototype instrument functioned well in the field except for a continuous, high frequency but low amplitude band of noise that affected all of the magnetic channels. This noise could not be filtered out and had the effect that processed data at periods below approximately 100 s were not usable. Four more second-generation instruments were built for use in the Gascoyne survey. They followed the design of the prototype but contained an adaptation intended to prevent the high frequency noise.

Although it had been planned that the five first-generation instruments and the five second-generation instruments would be available for the Gascoyne survey, hold-ups in another survey meant that the first-generation instruments

and the prototype second-generation instrument were still being used when Gascoyne field work began. The survey therefore had to be started with only four instruments. The remaining instruments arrived one week after field work began.

Methodology

Magnetic and electric recording axes were oriented at a default of geomagnetic north–south and east–west for data collection. Electric dipoles in these orientations were laid out with dipole lengths of approximately 20 m for first-generation instruments and 50 m for second-generation instruments. These dipoles were formed using three electrodes, one at the northern extent, one at the eastern extent and one acting as a common electrode, each with individual cables running to the logging electronics housed in the Pelican case (Fig. 6). Electrodes were buried to a depth of approximately 15 cm, such that the top of the electrode was level with the ground surface. The dirt in the bottom of the electrode hole was moistened with water to assist connection between the electrode and the ground. A ground electrode, consisting of a metal spike, was hammered into the ground and connected to a cable attached to the main Pelican case (Fig. 6).

Each Pelican case was buried to reduce visibility from passing traffic, to avoid disturbance by animals or wind and to reduce the range of temperatures affecting the magnetometer. The recording parameters were input to the instrument through a PC interface. This interface also allows data quality to be checked before the instrument starts recording. This process was used to orientate the magnetic sensor so that the magnetometer recording axes were directed north–south and east–west by minimizing the magnitude of the measured east-west magnetic field to within ±100 nT. Electric field magnitudes were also checked to be steady. First-generation instruments have an electric field threshold of ±25 mV while second-generation instruments have a threshold of ±250mV. If the field measurements were unsteady or off-scale, the electrodes were moved and reburied until the problem was rectified. Once these checks had been made the instrument was set to record.

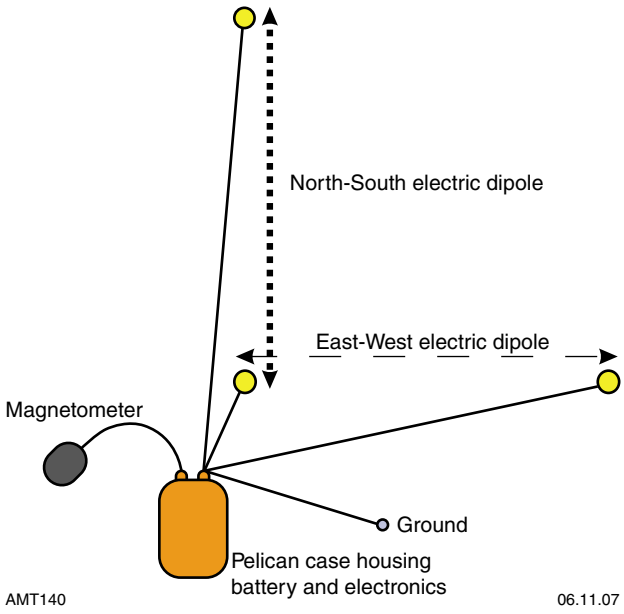

Figure 6. Schematic of instrument deployment for field data collection (not to scale). Electric dipoles are deployed in north–south and east–west directions and are standardized by a ground electrode. A magnetometer measures the magnetic field in the north–south, east–west, and vertical directions, and is housed in a separate Pelican case to the batteries and logging electronics. The Pelican cases are buried to a depth of ~50 cm and the electrodes are buried so that their top is approximately level with the surface

Final station locations

The original plan for data collection and station locations had to be amended in several ways. As stated above, although the survey had been planned with ten instruments available, only four instruments were available for the first week of field work. The other major problem discovered during field work related to the workings of the second-generation instruments. The four available second-generation instruments were deployed on the 6th September 2006, at the start of the field campaign. When they were retrieved on the 9th September, it was discovered that three of the instruments had turned off early in the recording period, one after recording for one hour, another after recording for four hours and the third after recording for thirty hours. Only one instrument had continued to record until it was manually turned off when it was retrieved. When these instruments were redeployed it was found that they all often, but not always, stopped recording before they were turned off. After the prototype arrived and was being used it was found to also exhibit the same behaviour. The cause for this behaviour could not be determined. It was intermittent, not occurring all the time for any instrument and the turn-off time would vary also. Instruments only ever stopped recording at the end of a block (or hour) of data. Testing showed that it was not related to battery charge. Discussions with the technician who had built the instruments could not reach the source of the problem. Most of the instruments were deployed several times, resulting in some stations with sufficient data and some with insufficient data for further analysis. Eventually it was decided that only two of the instruments, the prototype and one other, were reliable enough that they should continue to be used. The result of these malfunctions was that only seven instruments were used in the survey and that at several stations data were not collected for long enough to be useful in further processing and analysis.

Since extra field time had been allocated to allow for some instrument malfunction and failure of data collection, the original planned traverses could still be completed despite these malfunctions. However at some points station spacing was increased from the planned 5 km so that the survey could be completed within the available time. Again, this was not expected to significantly adversely

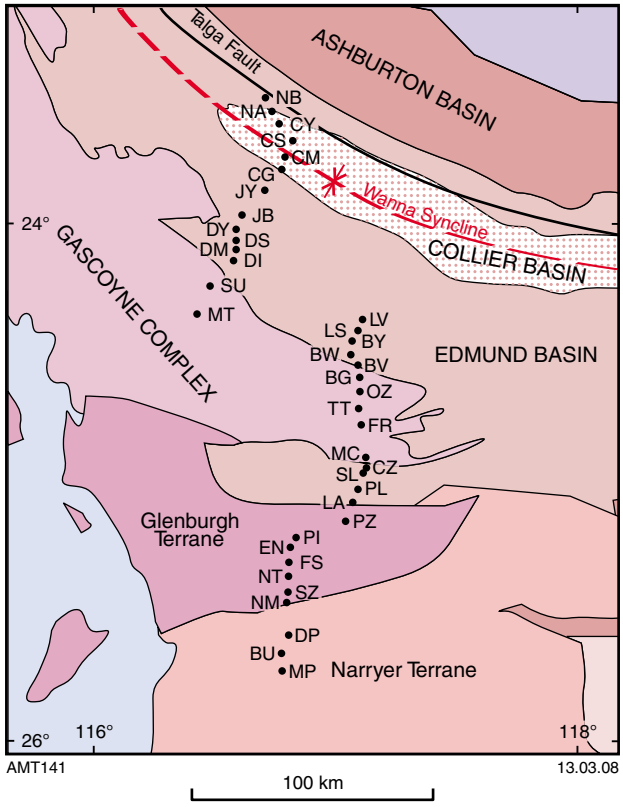

Figure 7. Locations and names of the stations where MT and/or induction arrow data were successfully collected and that were used in further analysis

affect the results since a station spacing of 5 km had been chosen for the very reason that, should spacing have to increase slightly or should data collection at a station fail, the spatial sampling would still be sufficient to image crustal- to lithospheric-scale features. The final station locations are plotted on Figure 7. The locations of all stations, including those that were not used in further analysis, together with the length of recording time and other data collection information are listed in Table 1.

Table 1. Locations, date recording commenced, record length, and instrument number for all stations collected

Station	*Eastings*	*Northing*	*Date commenced*	*Record length (hours)*	*Instrument*
SE	465424	7140204	9/09/2006	23	6140
MP	462887	7149200	9/09/2006	30	6139
BU	462626	7157010	13/09/2006	46	HFM3
FO	463013	7158746	6/09/2006	1	6136
FO (2)	463013	7158746	9/09/2006	96	6136
DP	465460	7164916	13/09/2006	48	HFM2
BT	466418	7168880	6/09/2006	4	6137
BT (2)	466418	7168880	09/09/2006	4	6137
BT (3)	466418	7168880	10/09/2006	4	6137
NM	468751	7173284	15/09/2006	45	4506
SZ	464746	7178803	6/09/2006	30	6139
NT	465146	7183647	12/09/2006	37	HFM4
SD	463525	7188589	6/09/2006	64	6140
FS	465948	7196189	12/09/2006	42	HFM1
EN	465995	7202737	12/09/2006	44	HFM5
PI	468187	7207227	13/09/2006	67	6139
PZ	487825	7214388	1/10/2006	47	HFM5
PR	487840	7214389	13/09/2006	20	6140
LA	490613	7222163	14/09/2006	68	HFM5
PL	492646	7228329	14/09/2006	67	HFM1
SL	495012	7235135	14/09/2006	67	HFM4
CZ	496078	7237487	1/10/2006	47	HFM3
CH	496073	7237502	19/09/2006	8	6137
MC	496098	7242207	15/09/2006	67	HFM2
CP	494647	7248990	15/09/2006	67	6136
FR	494106	7256225	16/09/2006	49	HFM3
TT	493060	7263284	16/09/2006	66	6139
OU	493439	7270105	16/09/2006	6	6140
OZ	493439	7270105	1/10/2006	47	HFM2
BG	492167	7278026	17/09/2006	85	HFM4
BV	492763	7282230	18/09/2006	91	HFM1
BW	490283	7286943	17/09/2006	95	HFM5
BY	490696	7292594	17/09/2006	97	4506
LS	493032	7297032	18/09/2006	93	HFM3
LV	494779	7301918	18/09/2006	78	HFM2
MT	428796	7303710	22/09/2006	44	HFM1
LY	493212	7307889	18/09/2006	91	6136
MN	427801	7309434	22/09/2006	44	6136
MA	488328	7312577	19/09/2006	11	6140
SU	434010	7315878	22/09/2006	65	HFM3
ST	442177	7321402	22/09/2006	17	6140
DI	443439	7327020	23/09/2006	72	HFM2
DM	444361	7331930	23/09/2006	71	4560
DS	444370	7335890	23/09/2006	50	HFM5
DY	444400	7340451	23/09/2006	71	HFM4
JB	446634	7346949	24/09/2006	68	HFM1
JS	451247	7353995	24/09/2006	68	6136
JY	455642	7357321	25/09/2006	47	HFM3
WI	459858	7362067	25/09/2006	2	6140
CG	462489	7266480	26/09/2006	77	HFM4
CM	463701	7372235	26/09/2006	92	4506
CS	466914	7379246	26/09/2006	96	HFM5
CY	461286	7386230	26/09/2006	93	HFM2
NA	458323	7391950	27/09/2006	73	HFM1
NB	456046	7397564	27/09/2006	71	HFM3
NO	453383	7400526	27/09/2006	60	6136

SOURCE: Caldwell et al. (2004); Cawood and Tyler (2004); Sheppart et al. (2003)

Processing

Data are recorded by the instruments as a time series of the magnitudes of the electric and magnetic fields. These time series data must then be Fourier transformed into the period domain, before outputs including impedance tensors, apparent resistivities, phases and induction arrows can be determined. Processing is the term that refers to these steps. The code Robust Remote Reference Magnetotellurics (RRRMT; Chave et al., 1987) was used to process all data in this project.

RRRMT uses robust statistics to remove non-Gaussian data outliers, such as dropped bits of digital data, spikes in the data or magnetic storm signal affecting the geomagnetic field. Robust techniques are efficient because they are insensitive to a moderate amount of contaminated data and react gradually rather than abruptly to disturbances in the data (Chave et al., 1987). The robust methods implemented by RRRMT operate in an automatic, data adaptive fashion that breaks down only in unusual circumstances (Chave et al., 1987). RRRMT uses a remote reference (Gamble et al., 1979a–c) to reduce incoherent noise (Chave and Thompson, 1989). Figure 8a shows that at low periods

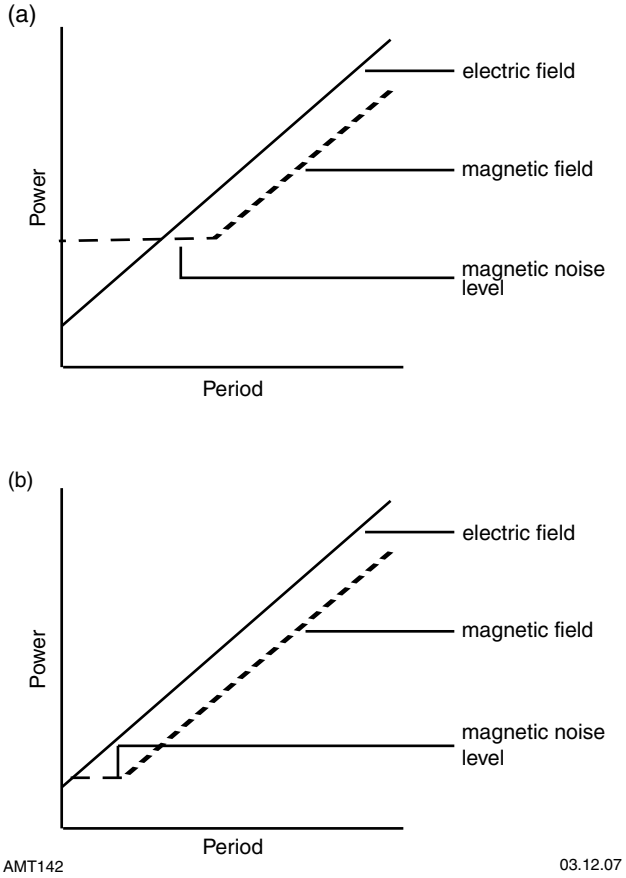

Figure 8. a) at short periods the power level of magnetic noise is greater than that of the magnetic signal, leading to a sharp drop off in apparent resistivity estimates; b) the addition of a remote reference removes incoherent noise and lowers the level of magnetic noise, causing to drop in apparent resistivity to occur at a lower period

the magnetic field is dominated by noise since the power level of the noise is greater than the power of the signal. This has the result that apparent resistivity, which is proportional to the square of the electric field divided by the magnetic field, becomes very small at low periods. To address this, remote magnetic field measurements are taken at a reference point some distance away from the site of primary magnetic field measurement. Differences between the remote and primary magnetic field measurements are taken to be incoherent noise and are downweighted or removed from the data. This lowers the amplitude of the magnetic noise (Fig. 8b) with the result that the values of apparent resistivity do not fall off until a significantly shorter period.

Quality of recorded data from first- and second-generation instruments

First pass processing of data from the first-generation instruments was carried out in the field to check data quality, which was generally good. It had been noted in previous surveys that the prototype second-generation instrument often skipped writing the second line of data to file in a block. Data are saved in files or 'blocks' that each contain one hour of data, with each line of data in the block representing one second. First-pass processing of data from the prototype instrument was able to be carried out in the field because processing codes had been adapted to account for the skipped lines. Data quality was good, although the high frequency band of noise that had been seen in earlier surveys was still affecting the magnetic channels, as had been expected. While the prototype instrument only ever skipped writing one line of data at the start of a block, it was found that the other second-generation instruments would skip up to four lines of data in each block. These skipped lines were distributed randomly in the block. This problem was intermittent and in some blocks no lines of data were skipped. The processing codes required that each block contain 3600 seconds (or lines) of data and could not be adapted in the field to allow for first-pass processing of data from the four newest second-generation instruments. Since data from the prototype instrument was of good quality and the other second-generation instruments had followed its design, it was presumed that data from these other instruments would also be of good quality.

After the field work was finished the behaviour of the second-generation instruments was analysed closely. The processing codes were adapted to allow the data to be processed despite the skipped lines of data. Unfortunately, it was discovered that there were serious problems with the data these instruments recorded. The adaptation that had been included to prevent the high-frequency noise from affecting the data had not worked, and the recorded magnetic fields were still affected by this noise. Additionally, the magnetic fields themselves were often recorded incorrectly, but this varied between instruments. In some instruments the problem was simply that one of the fields was inverted, that is, if the field magnitude was multiplied by –1, the correct field amplitudes were regained. However in other instruments the recorded magnetic fields bore no similarity to magnetic fields recorded at the same time but at a different location. This showed that serious problems existed in the instrument's recording of the magnetic fields since they should be almost identical to those at the different location. Further processing with the data from such instruments confirmed that the fields were recorded incorrectly as no coherent or usable MT data was produced.

An assumption of MT is that the magnetic field is propagated from a distant source and arrives at the surface of the earth as a plane wave. The primary magnetic field should therefore be the same at two locations on the earth spaced several kilometres apart. For this reason, in most circumstances, if data collection of the magnetic fields fails at an MT station, the magnetic fields recorded at another station at the same time should be able to be substituted in with no associated loss of data quality. This process was attempted for the stations with data collected by the instruments described above which did not record the earth's magnetic field accurately. However, substituting in an alternative set of magnetic field measurements did not produce good quality data at these stations. Indeed,

no improvement was made to the processed data. This suggests that not only were the magnetic fields affected, but the electric fields were also recorded incorrectly, even though the data quality and signal strength of the time series appeared fine. It is more difficult to check whether electric fields have been recorded correctly since they should change from station to station and cannot be directly compared.

The results of this analysis were that the second-generation instruments that simply inverted one or more magnetic channel produced data that could be used for further processing, provided the affected channels were edited. Specifically, these instruments were 4506 (the prototype) and 6139 (Table 1). The logged magnetic data that bore no resemblance to the actual magnetic fields, and the associated electric fields, could not be used in any way. The instruments that logged such data were 6136, 6137, and 6140. These problems were due to serious faults in the manufacture of the instruments and could not have been rectified in the field, even if the data had been taken through first-pass processing.

In summary, the main problems with the second-generation instruments were:

1. Instruments turned off during recording
2. Instruments skipped recording lines of data
3. Instruments 4506 and 6139 inverted some magnetic channels during recording, which could be rectified during further processing
4. Instruments 6136, 6137, and 6140 recorded the magnetic and probably the electric fields completely incorrectly and did not produce any data that could be used in further processing.

A total of eighteen stations were thus removed from further processing. Ten of these would not have been able to be used for processing anyway since the instrument had turned off early in the record and a total of twenty hours or less of data had been recorded.

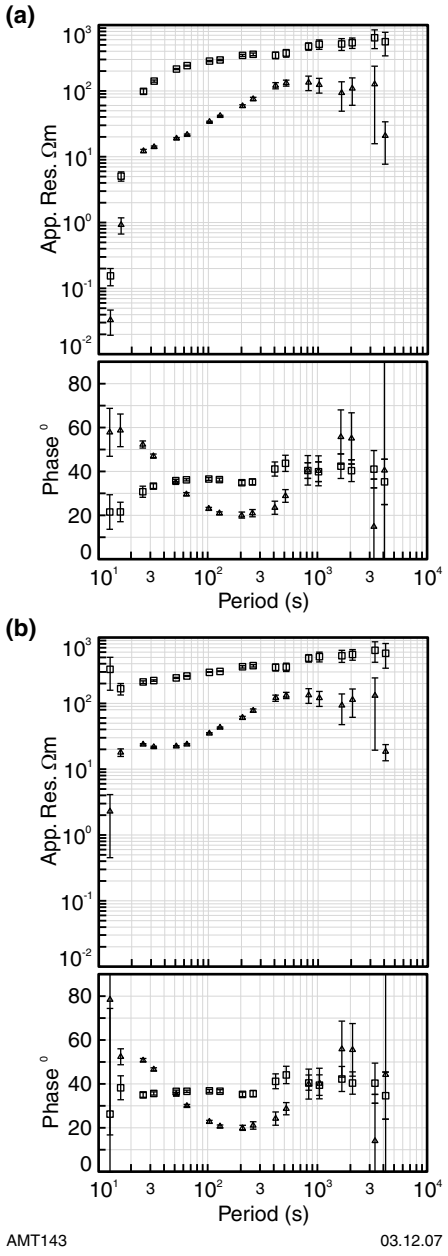

Figure 9. Processed data from station FS before (a) and after (b) remote referencing. Remote referencing has removed the sharp drop off in apparent resistivity values at periods less than approximately 30 s by improving the signal to noise ration of the magnetic field

Processing results

The remaining 38 stations were fully processed using RRRMT (Chave and Thompson, 1989; Chave et al., 1987). All stations were remote referenced with the magnetic fields of a simultaneously recording station. This had the effect of improving the signal to noise ratio, reducing the size of error bars on the apparent resistivity data and reversing any decreases in the magnitude of apparent resistivity at short periods due to the dominance of the power level of the noise at these periods (Fig. 9).

Induction arrow data were produced at all 38 stations. Data are of a consistently good quality along the line and are in the period range of approximately 10 to 4000s. Real induction arrow magnitudes and directions at periods of 100, 500, 1000, and 2000s are shown in Figure 10.

Processing produced apparent resistivity and phase data at 27 of the 38 stations. At three stations apparent resistivity and phase information could not be produced because the electric field recording had failed, either through going off scale or through disconnection of electrodes early in the record. The northernmost six stations produced apparent resistivity and phase data of such poor quality that they could not be used. Apparent resistivity and phase data from stations DI to NB, which are at the north of the profile, are shown in Figure 11. There appears to be a gradual decrease in data quality from approximately station DI northwards, as demonstrated on Figure 11 by phases which plot outside of the ±90° scale, apparent resistivity and phase values with very large error bars and apparent resistivity

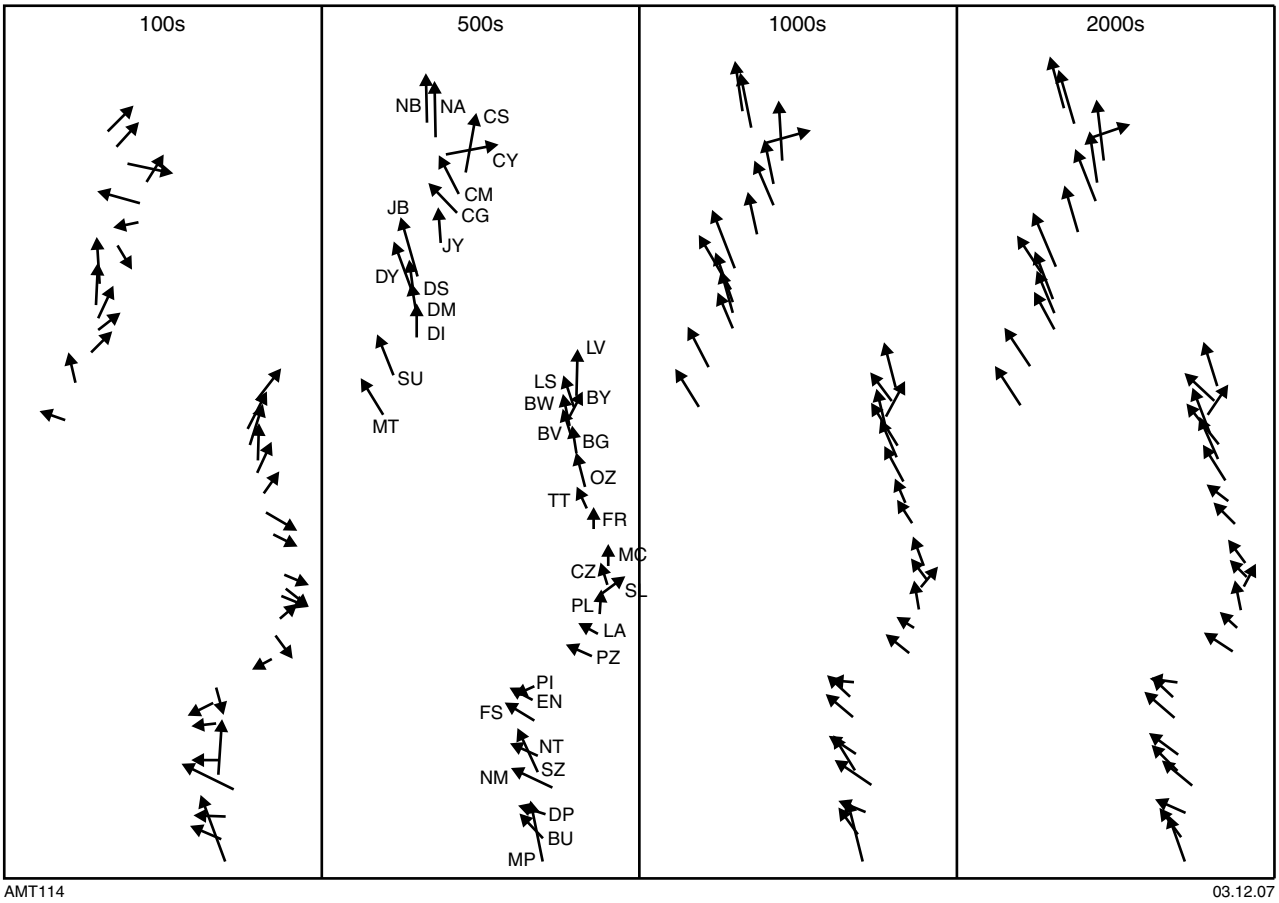

Figure 10. Induction arrow data from stations along the profile at periods of 100 s, 500 s, 1000 s, and 2000 s

and phase values that do not vary smoothly with period. Stations north of JY did not produce any usable quantity of apparent resistivity and phase data (Fig. 11). These stations lie in an area of significant topographic complexity in the Bangemall Supergroup. The topography is characterized by significant ridges of sedimentary lithologies cut through with riverbeds which are often flanked by steep cliffs (Fig. 12). Electric field recording failed at the remaining two stations for unknown reasons.

Dimensionality analysis

For MT data to be modelled along a profile with a 2D inversion scheme, the data must, to a reasonable extent, respond to a subsurface that is geoelectrically 2D (or 1D). A 2D subsurface has resistivity variations in two directions but not the third. It could be represented by, for example, a subsurface with a dipping fault that separates regions of differing resistivities but with a strike direction that is constant, such that resistivity changes with depth and across strike, but not along the strike of the fault. If the subsurface differs dramatically from this, for example by having conductivity structures that have finite strike lengths or significantly different strike directions with depth or laterally, 2D inversion of the data will result in spurious features being modelled. The data must therefore be examined to determine the electrical dimensionality of the subsurface and the geoelectric strike direction before any modelling can be undertaken. A further complication that can affect the data is galvanic distortion, where near-surface electrical features distort the deeper data (e.g. Groom and Bailey, 1991). Galvanic distortion can make regional 2D electrical structures appear 3D as the currents and fields are distorted along near-surface features. The underlying regional conductivity structure can be irretrievable from data severely affected by galvanic distortion.

The dimensionality of the data was analysed using the phase tensor. The phase tensor (Bibby et al., 2005, Caldwell et al., 2004) determines the dimensionality and geoelectric strike direction of MT data by analysing the phase, rather than the apparent resistivity, as it is unaffected by galvanic distortion. Phase tensor analysis allows a determination of the dimensionality of the subsurface without the need for assumptions that the regional structure is 1D or 2D and is affected by galvanic distortions, which underlie other decomposition techniques (e.g. Bahr, 1988).

The phase tensor is defined as

$$\Phi = \begin{bmatrix} \Phi_{11} & \Phi_{12} \\ \Phi_{21} & \Phi_{22} \end{bmatrix} \tag{28}$$

and by the relationship (Caldwell et al., 2004)

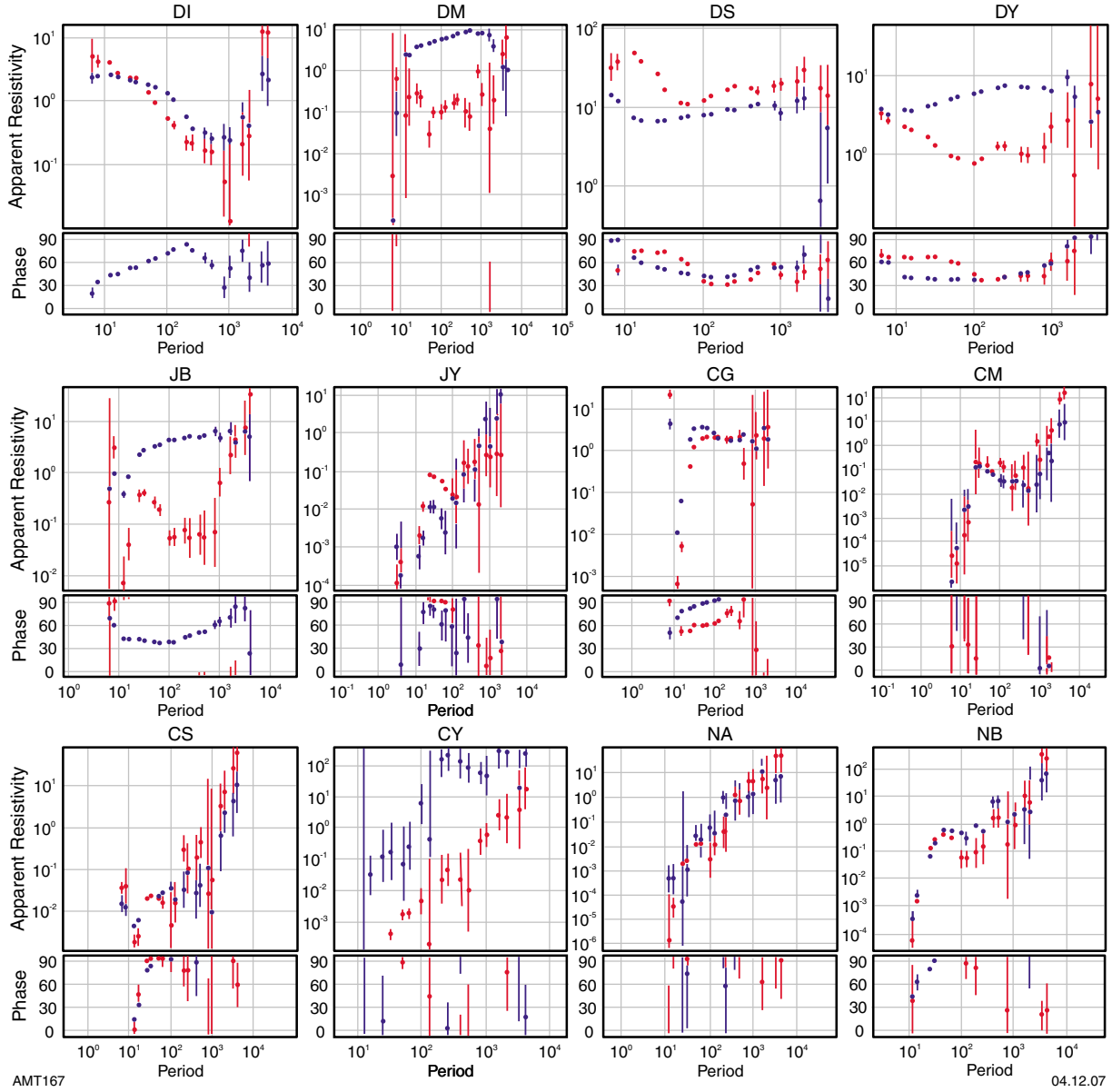

Figure 11. Apparent resistivity and phase data from stations on the Bangemall Supergroup, extending north from station DI to station NB. The very large error bars on many of these data points and the fact that many of the phase values plot outside of the ±90° range suggests that these data are severely distorted

Figure 12. Photo looking north towards Coodardo Gap in the Bangemall Supergroup. Coodardo Gap is approximately coincident with station CG. The significant topography in the region, consisting of strike ridges and riverbeds, is the probable cause of the distortion of the MT data

$$\Phi = X^{-1}Y \tag{29}$$

where X and Y are defined from the impedance tensor Z through the complex tensor relation Z=X+*i*Y.

The phase tensor is characterized by three values which are invariant on rotation, the maximum (Φ_{max}) and minimum (Φ_{min}) phase values and the skew angle β. The skew angle is a measure of the tensor's asymmetry and therefore of dimensionality. It is given by the relation

$$\beta = \frac{1}{2}\tan^{-1}\left[\frac{\phi_{12}-\phi_{21}}{\phi_{11}+\phi_{22}}\right] \tag{30}$$

The fourth parameter that defines the phase tensor is the angle α that expresses the tensor's dependence on the coordinate system.

$$\alpha = \frac{1}{2}\tan^{-1}\left[\frac{\phi_{12}+\phi_{21}}{\phi_{11}-\phi_{22}}\right] \tag{31}$$

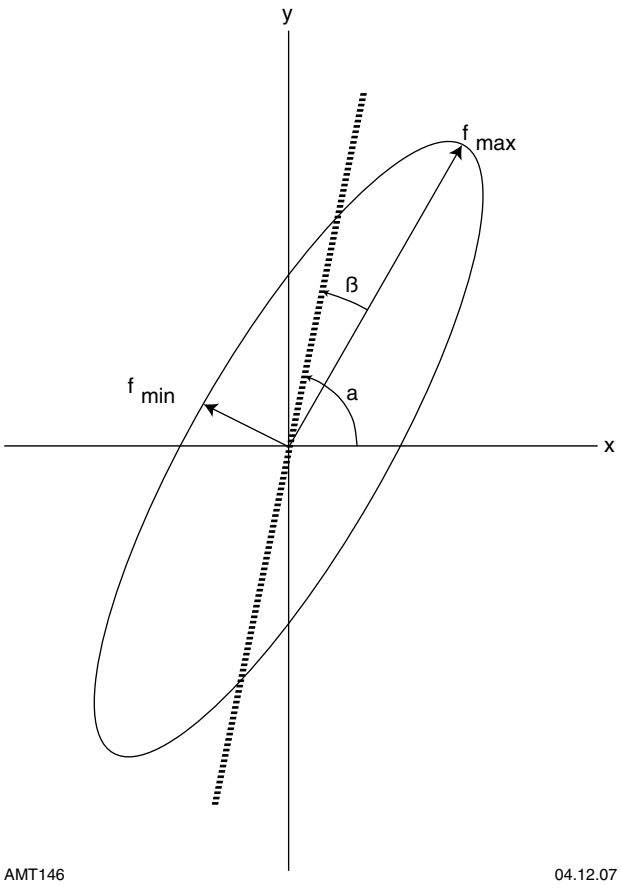

Figure 13. Graphical representation of the phase tensor as an ellipse, from Caldwell et al. (2004). The relation (α–β), where the skew β is a measure of dimensionality, gives the direction of the major axis of the ellipse Φ_{max}, which shows the relationship of the direction of maximum current flow to the observation axes x and y

The phase tensor is commonly represented as an ellipse, as demonstrated in Figure 13. In 1D or 2D settings, the skew angle β equals zero, the tensor is symmetric and the orientation of the major axis of the ellipse is given by α. In other settings, the orientation of the major axis is given by α-β.

A 2D tensor is represented by an ellipse and should have skew values less than approximately five degrees. The azimuth of the major axis of the phase tensor is related to the maximum direction of current flow in the earth and should therefore be period-independent in a 2D setting. Indeed, the authors suggest that this is a better indicator of 2-dimensionality than a low skew value. However at periods where Φ_{max} and Φ_{min} are similar, the azimuth is ill-defined and is itself an unreliable indication of dimensionality. In a 3D setting, the azimuth will be period-independent and $\beta \neq 0$.

Figures 14, 15, and 16 show phase tensor data for all stations along the profile, extending from south to north. The skew (Fig. 14) is the angle β (Equation 30) that is a measure of the dimensionality of the data. A skew angle with magnitude less than 5° suggests that the subsurface is either 1D or 2D. The strike angle (Fig. 15) is a determination of the geoelectric strike. Since a 1D subsurface has no strike direction, the phase tensor strike of a 1D region is ill-defined. The phase tensor strike of a 2D region will be consistent with period and at different stations along the profile. A 3D subsurface will produce strike directions that are period-dependent and station-dependent. The strike direction contains an inherent 90° ambiguity since it is impossible mathematically to distinguish between along and across strike MT responses. The eccentricity (Fig. 16) is a measure of how elliptical the phase tensor is. This is a useful measure of one-dimensionality since phase tensors of a 1D subsurface approximate circles. Eccentricities of less than 0.1 suggest one-dimensionality.

Analysis of the phase tensor data suggests that the profile can be separated into four groups of stations, each with individual dimensionality and strike characteristics. From south to north, these groups are as follows:

Station MP to station SZ

From station MP in the south to station SZ in the north, there are four stations, NM, DP, BU, and MP, which possess data that can be fully analysed for dimensionality. Station SZ contains only TE mode data so a full analysis cannot be carried out. All of the phase tensor data suggest that this region is 3D. The strike angle data show significant variation with period. Some of this variation can be explained by a 180° uncertainty in strike direction, such that a strike of -180° is equivalent to a strike of 180°, however with this taken into account there remains a change in strike of approximately 50° with period. Skew values are generally dominated by large error bars. Since the error bars generally cross at least part of the range between -5° and 5°, it is possible that the skews are in the two-dimensional range and merely denote poor data quality rather than three-dimensionality. However the skews at station BU are much better constrained and

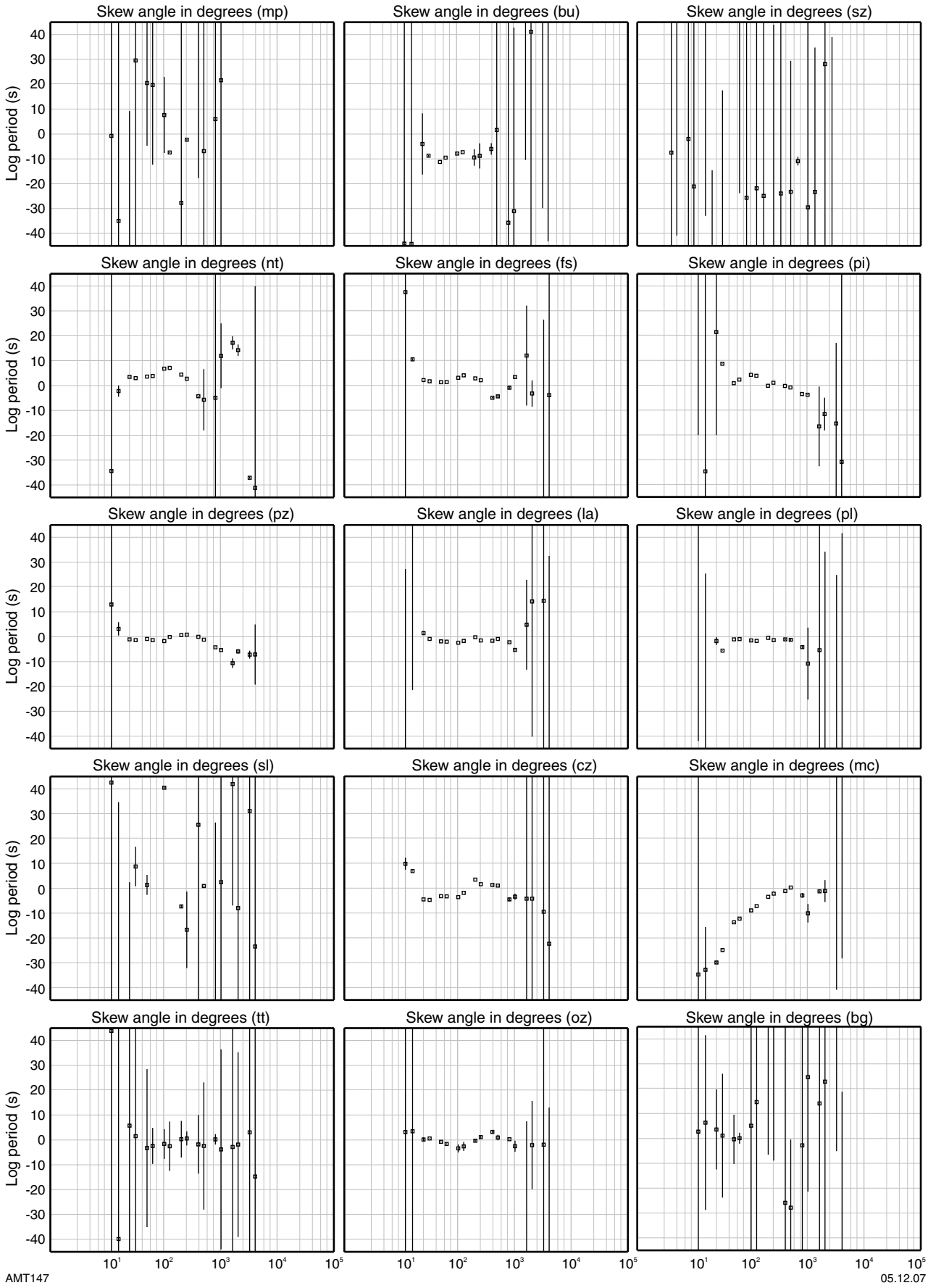

Figure 14. Plots of the phase tensor skew against period for all stations on the profile, arranged from south (mp) to north (cg). Skew is a measure of dimensionality, and should be less than ±5 in a 2D or 1D setting

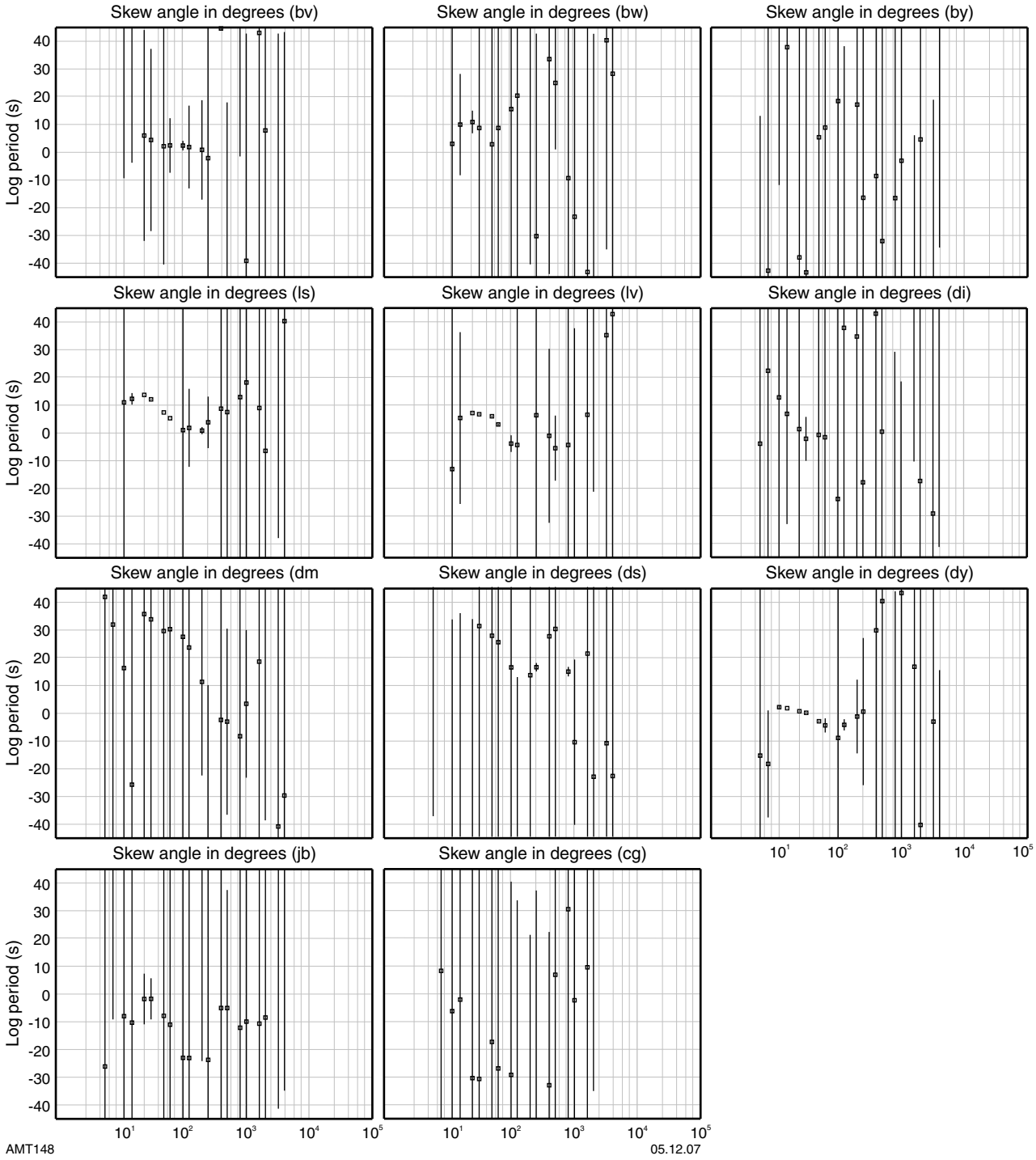

Figure 14. (continued)

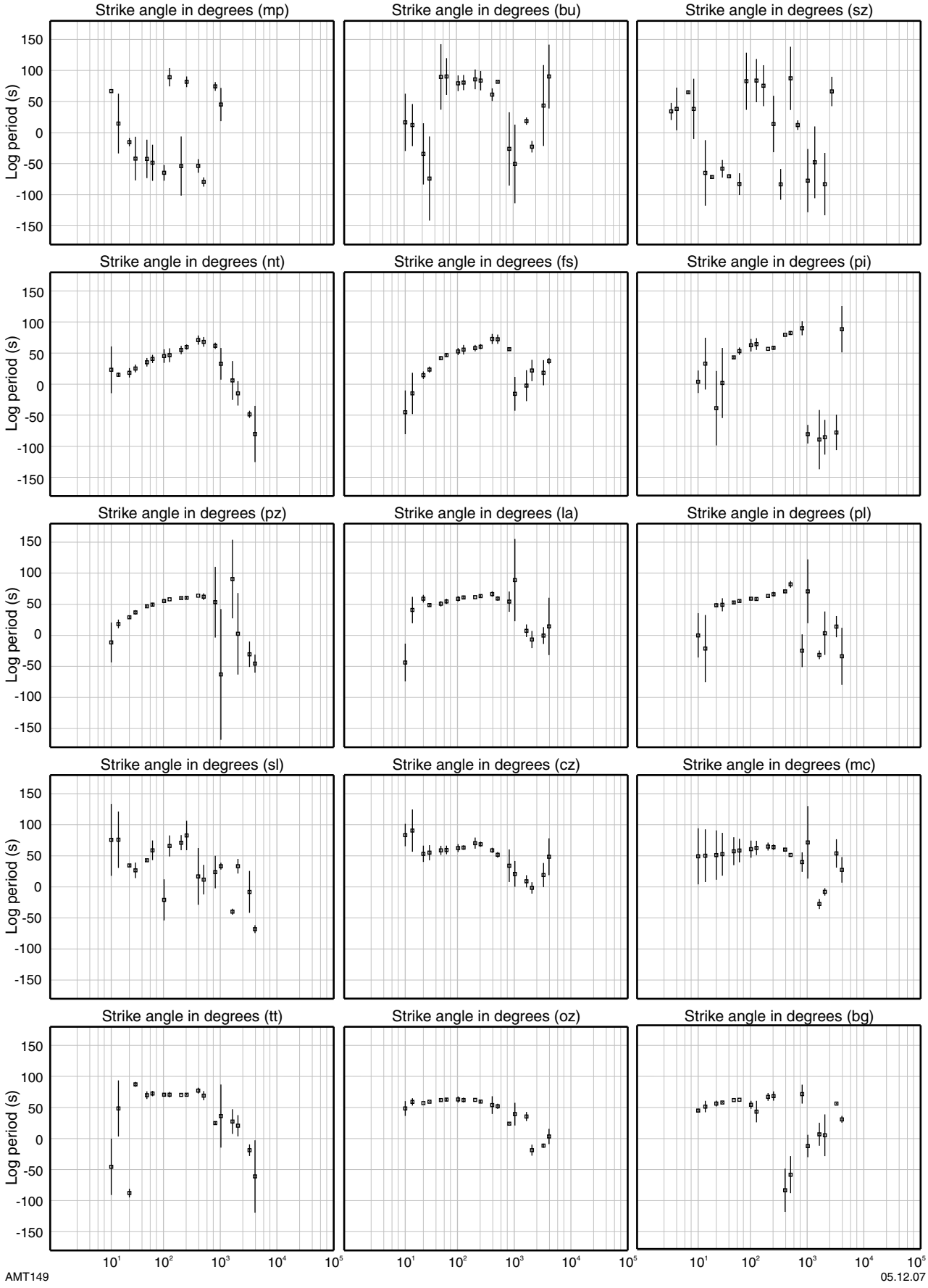

Figure 15. Plots of the phase tensor strike against period for all stations on the profile, arranged from south (mp) to north (cg)

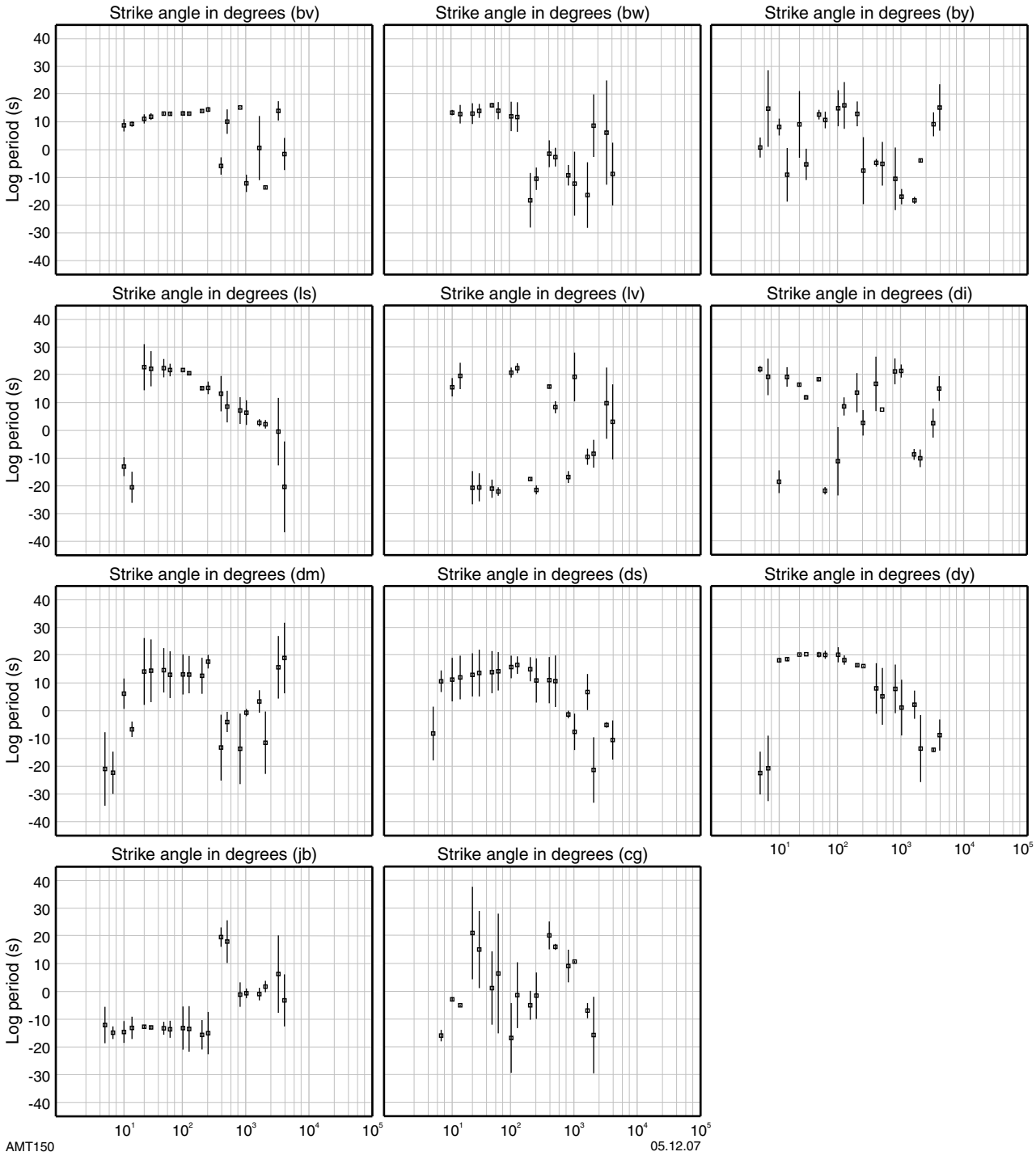

Figure 15. (continued)

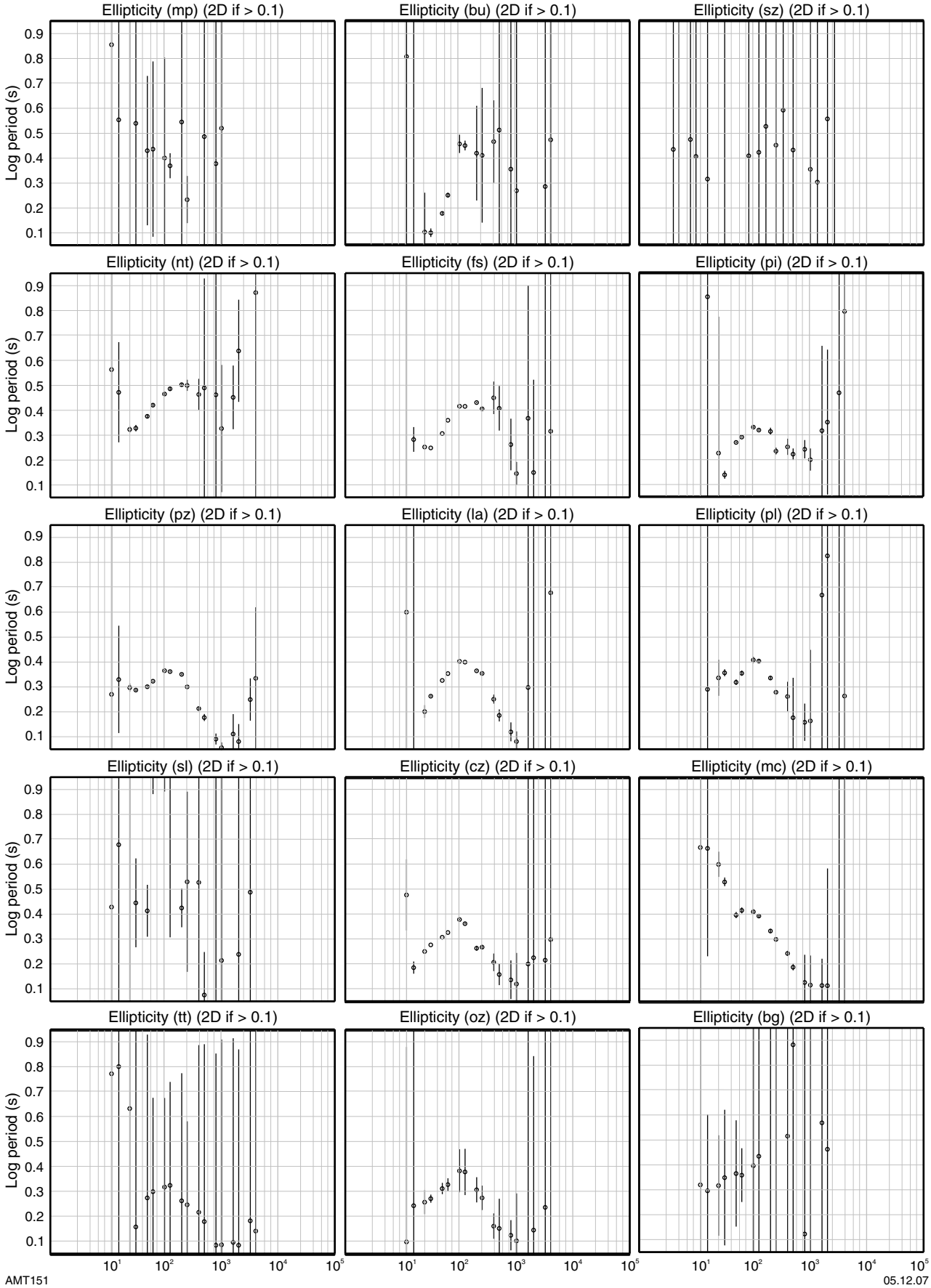

Figure 16. Plots of the phase tensor eccentricity against period for all stations on the profile, arranged from south (mp) to north (cg). Eccentricity is a measure of how strongly the electrical currents prefer to flow in one direction over another. Eccentricities of less than 0.1 suggest one-dimensionality

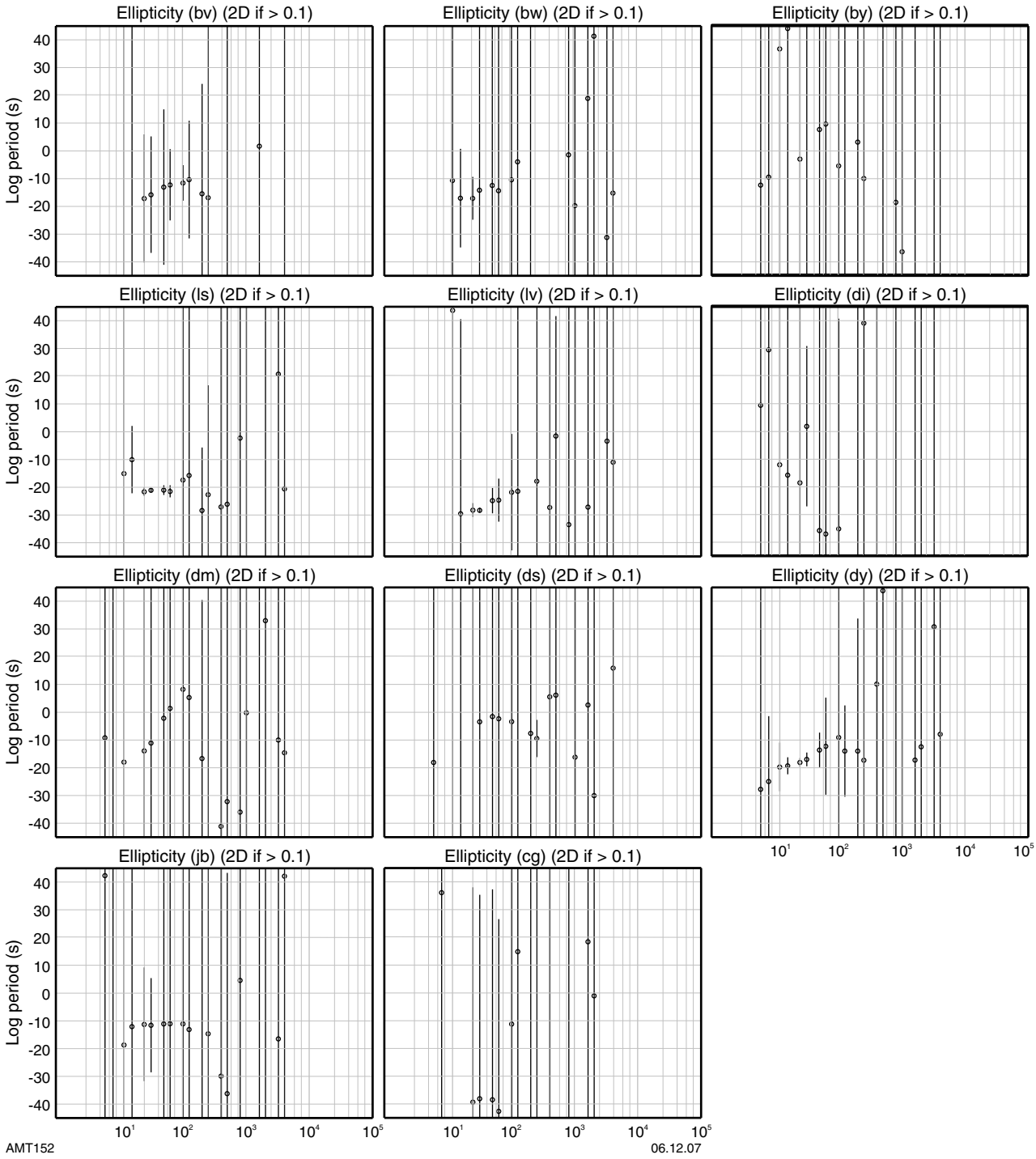

Figure 16. (contined)

have magnitudes between 10 and 5, suggesting that the underlying subsurface is electrically three-dimensional. The combination of this with the period-dependent strike angles suggests that this region should be considered 3D.

Station NT to station BW

The phase tensor data of station NT in the south to station BW in the north are quite consistent. The most variation in phase tensor strike, both with period and at different stations, is at periods less than ~100 s. In the north of this section, particularly from station LA to station BW, phase tensor strikes at periods less than ~100 s are quite consistent and period-independent and average at between 50° and 60°. However in the southern part of this section, between stations NT and PZ, the phase tensor skews are more period-dependent and trend on average from ~20° at ~20 s to ~50° at ~100 s. The magnitude of this period dependence decreases from south to north along this section. Most of the phase tensor skews for this range between stations NT and PZ are between ±5°, indicating 2-dimensionality, but the period-dependence of the strikes shows that these data points actually denote 3-dimensionality. These data suggest that at periods less than 100 s, 2-dimensionality increases from south to north from station NT to PZ and that the subsurface is quite 2-dimensional from station LA to BW.

Between periods of ~100 s and ~700 s from station NT to station BW, phase tensor strikes are reasonably period-independent and consistent between stations. The average value of the phase tensor strikes is approximately 60°. Most of the phase tensor skews for this period range are between ±5°. These data all suggest that at these periods, the subsurface is 2D.

At periods greater than ~700 s from station NT to BW, the phase tensor strike becomes quite erratic. Skew values are quite variable from station to station, with some being quite erratic or having large error bars, but others sitting between ±5°. Eccentricity plots also show some variation. Data from some stations are erratic and have very large errors, but data from many stations show that eccentricities in this period range drop below a value of 0.1. This suggests that the data are 1D and explains the sudden inconsistency of strike data, since the strike in a 1D area is undefined.

Station BY to station JB

The phase tensor analysis of these stations is hampered by the dominance of very large errors in most of the data. Phase tensor strike directions show a consistent trend of averaging at approximately 60° at periods less than ~200 s before dropping down in magnitude to approximately 0° at ~1000 s, while becoming more erratic and having increasing errors. Almost all skew values are completely dominated by large errors. Where skew values with small errors do exist (specifically at stations LS, LV, and DY), their values are inconsistent and do not provide a uniform indication of the dimensionality of the subsurface. Most eccentricity values are also dominated by errors, but usable data points show eccentricity values of between approximately 0.2 and 0.4. The available data do not therefore suggest one-dimensionality and this can not be used as an explanation for erratic strike angles. Data points at shorter periods with consistent strike directions at approximately 60° and skew values that at least have error bars that lie in the range between ±5° could be considered to be 2D.

Station JY to station NO

As described above, no useful apparent resistivity or phase data were produced for these stations, so a full dimensionality analysis is impossible.

Correlations with geological regions

There are several areas in which major changes observed in the behaviour of the phase tensor or induction arrows corresponds to changes between geological regions as recognized on the surface:

Outcropping Yilgarn Craton/outcropping Gascoyne Complex across the Errabiddy Shear Zone: At the surface, the boundary between the Yilgarn Craton and the Gascoyne Complex is marked by the Errabiddy Shear Zone. The MT profile crosses the Errabiddy Shear Zone near station SZ. Stations MP to NM lie on outcropping Yilgarn Craton and stations NT to BW lie on outcropping Gascoyne Complex. At periods less than ~100 s, induction arrows show a slight reversal across the Errabiddy Shear Zone, with arrows to the south of it pointing to the northeast and arrows at stations NT and TT to the north of it pointing toward the southeast (Fig. 10). The arrow at station SZ points approximately along the strike of the Errabiddy Shear Zone. This behaviour suggests that at the depths corresponding to the affected periods, the Errabiddy Shear Zone is a more conductive feature than the surrounding subsurface.

The phase tensor data suggest a significant electrical difference between the Yilgarn Craton and the Gascoyne Complex. Phase tensor data from stations on the Yilgarn Craton suggest that the region is electrically 3D. Stations on the Gascoyne Complex show much more evidence of 2-dimensionality. Stations show increasing 2-dimensionality with distance from the Yilgarn and, at stations close to the Yilgarn, it is the shorter period data that show 3-dimensionality, suggesting that these stations are being affected by the 3-dimensionality of the Yilgarn as the recorded fields penetrate into it.

Gascoyne Complex

Stations NT to BW lie on outcropping Gascoyne Complex. Apart from phase tensor data suggesting 3-dimensionality at periods less than 100 s at stations toward the south of the Gascoyne Complex, which is probably due to proximity to the Yilgarn Craton, the phase tensor data from the Gascoyne Complex suggest that it is 2D, trending to more 1D at depths corresponding to periods greater than 700 s (Figs 14–16). This analysis is supported by the induction arrow data (Fig. 10). Induction arrows in the central Gascoyne Complex, especially from station CP to BG, have very small magnitudes of ~0.1 at periods longer

than ~500 s. This shows that the arrows are not responding to significant resistivity gradients (which would result in a larger magnitude) and supports the interpretation of one-dimensionality at depth beneath the Gascoyne Complex.

Bangemall Supergroup

Stations BY to NO lie on outcropping Bangemall Supergroup. Analysis of apparent resistivity and phase data from these stations led to the suggestion that the topography had led to a severe distortion of the data (Fig. 11). Phase tensor analysis supports this suggestion, with phase tensor data even from the more southerly stations that produced reasonable MT data showing significant irregularity (Figs 14–16). The change from the consistent 2D or 1D data from more southerly stations to this irregular data coincides with the beginning of outcropping Bangemall Supergroup.

Modelling

Data were modelled using the inversion code non-linear conjugate gradients (NLCG; Rodi and Mackie, 2001) included in the software package WinGLink, published by Geosystem. The NLCG technique is described in Polak (1971) and Luenberger (1984). One of the most computationally expensive operations in 2D MT inversion is the determination of the Jacobean (e.g. de Groot-Hedlin and Constable, 1990). Mackie and Madden (1993) show that operations with the Jacobean and its transpose can be achieved without having to actually compute the Jacobean itself using the method of conjugate gradients. The NLCG algorithm proceeds from this premise and abandons the structure of iterated and linearized inversions. Instead, NLCG performs a sequence of line searches along computed search directions to solve the minimization problem.

The fit of the model data to the station data is reported as a root mean squared (rms) difference between model and station data points for all parameters included in the inversion (apparent resistivity, phase, and/or vertical magnetic field). As for all MT data, a perfect data fit can be obtained if the model is permitted to contain sufficient structure, although a realistic model is limited in detail by the resolving power of the technique. For the purposes of interpretation, a smoother model that contains reliable structure is preferable to a less smooth model that contains unrealistic structures. For this reason the Rodi and Mackie (2001) algorithm contains a regularization parameter tau (τ) that acts as a trade-off between smoothness and model fit. Larger values of τ create a smoother model at the expense of data fit, while smaller values of τ produce a rougher model with a better data fit.

2D MT inversion

2D inversion is the process of converting apparent resistivity, phase and/or vertical magnetic field against period data from individual stations to a cross-section of resistivity against depth for an entire profile. Since MT is a volume sounding method, data from any depth greater than the station spacing will be recorded by more than one station. Inversion integrates the data from all stations, producing a much more reliable model than simple stitched 1D inversions for each station. 2D inversion proceeds under the assumption that the strike of modelled features is infinite and that no electrical bodies exist out of the plane of the profile that affect the data.

Data inclusion

Full 2D MT inversion can only be carried out where (1) MT data have been successfully collected and (2) dimensionality analysis shows that the data are 2D. As described in the previous section, these criteria exclude much of the data collected along this profile. Many of the data, particularly those at the southern end of the profile, are 3D and therefore should not be modelled under a 2D scheme. Stations on the northern end of the profile also show evidence of 3-dimensionality but also are very distorted and have not produced good quality MT data. Inclusion of such data into a 2D model may result in the modelling of spurious features. Therefore, from the groupings observed in the phase tensor data:

- data from station MP to station SZ were considered 3D and not included in inversion
- data from station NT to station BW were generally considered 2D and were included in inversion. Individual data points were either included or excluded depending on whether the phase tensor analysis suggested it was 2D or not. In particular, data from periods shorter than 100 s from the southern part of this section were not included due to the period-dependence of their phase tensor strikes.
- phase tensor analysis of stations BY to JB showed evidence of 2-dimensionality at shorter periods, trending into 3-dimensionality at longer periods, with the 3-dimensionality increasing northwards. Only shorter-period data from stations LS and LV were included in inversion since stations further to the north contained at most three data points that could be considered 2D, which was insufficient to generate a robust model.
- data from station JY to station NO were too distorted to be able to run dimensionality analysis and could not be included in inversion.

Strike direction

The MT data were collected with axes oriented north–south and east–west. However, for 2D inversion the axes must be mathematically rotated to be parallel and perpendicular to the geoelectric strike. Inversion should then be carried out along a profile that is perpendicular to geoelectric strike. Phase tensor analysis showed that, throughout the region shown to be 2D, the average geoelectric strike direction is 60° (Figs 14 and 15). Strike direction became erratic in the region considered to be 1D (Figs 15 and 16), but since strike is by its nature undefined in a 1D region, these data can be rotated in the manner as the 2D data.

There is an inherent 90° ambiguity in the geoelectric strike direction because it is impossible mathematically

to determine whether it is the TE or the TM mode that should be oriented along this line (Caldwell et al., 2004). It is only through analysis of additional information that this ambiguity can be resolved. The mapped strike of geological features in this region does not fully resolve this since strike directions similar to 060° (such as the Errabiddy Shear Zone) and to 120° (such as the Talga and Chalba Faults) are evident (Fig. 1). Induction arrows respond only to geoelectric structure and are therefore useful for constraining geoelectric strike. In general in a 2D setting induction arrows point perpendicular to geoelectric strike. Although there is some variation in the direction of induction arrows at periods shorter than approximately 200 s, at longer periods the arrows point consistently north/north-west (Fig. 10), supporting a strike of 060°. Station data were therefore rotated 30° anticlockwise using RRRMT so that the TM mode was perpendicular to strike and the TE mode parallel. The data were modelled along a profile oriented perpendicular to strike.

Inversion results

A 2D inversion was run with a starting uniform half-space of 100 Ωm and a tau of 3. To account for static shift effects, static shift was included as an inversion parameter (under the datum that the ln of the static shifts should sum to zero) and additionally the apparent resistivity error floors were set to 30%, while phase error floors were set to 1.45°.

The model inverted to an rms of 3.78 and is shown to a depth of 60 km in Figure 17. The two main modelled conductive features, labelled A and B on Figure 17 have resistivities less than approximately 120 Ωm. Feature A lies beneath stations LV to TT and, although it reaches the surface from station BW to BV, dominantly extends from a depth of approximately 10 km to 35 km. In contrast, feature B extends to the surface at most points and extends to a depth of approximately 20 km. The detail modelled in the top 5 km of the model is probably more structured than the data can support and should not be over-interpreted. A more resistive feature labelled C, with resistivity up to approximately 2500 Ωm, separates features A and B. Beneath A and B is a more resistive region D with resistivity between approximately 140 and 350 Ωm. The NLCG inversion code in WinGLink often models more resistive bands between stations and less resistive bands beneath stations. This is the probable explanation for the thin vertical bands with resistivities of approximately 120 Ωm that extend beneath all stations to at least the upper mantle depths displayed. This is also a possible explanation for the existence of the resistive feature C since it lies in a significant, approximately 20 km long gap between stations TT and MC.

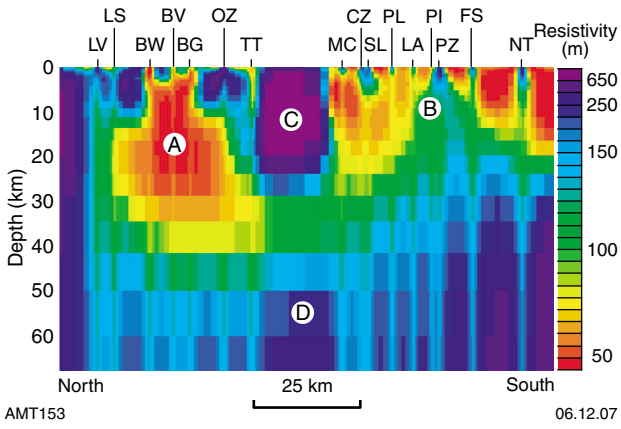

Figure 17. The 2D MT model of data determined to be 2D by phase tensor analysis inverted to an rms of 3.78. Two main low resistivity features, labelled A and B, have been modelled. These features are separated by a high resistivity feature C and underlain by another high resistivity feature D

Model tests

As mentioned above, several features were evident in the initial model that may not have been required by the data: specifically, (1) the detail modelled in the uppermost 5 km, (2) the resistive region C that lies in a gap between stations, and (3) the vertical bands with approximate resistivities of 120 Ωm that extend to depth beneath all stations. These features should be tested to determine whether they are required by the data or are simply a modelling artefact. Additionally, the possible geological interpretation of the model requires that further testing be carried out. The boundary between the Glenburgh Terrane and the northern Gascoyne Complex along the profile line is at the Chalba Shear Zone, which runs through the gap between stations TT and MC. The relationship between the Glenburgh Terrane and the northern Gascoyne Complex is unknown, but one possibility is that the Glenburgh Terrane forms basement to the northern Gascoyne Complex. This may be supported by the current model, which shows a conductive band (B) in the Glenburgh Terrane that drops down to a greater depth in the northern Gascoyne Complex (Feature A). The depth extent and the depth to the top of features A and B should therefore also be tested to determine whether the data require a vertical offset between these two features.

A single model test was run which incorporates all of the above features. The top 15 km across the whole of the model space was set to 500 Ωm, testing for both the robustness of the detail modelled in the uppermost 5 km and for the depth to the top of the conductive regions A and B. Below 30 km depth, the resistivity of the whole model space was set to 700 Ωm to test the depth extent of features A and B and also to test the vertical 120 Ωm bands beneath the stations. The resistive feature C was tested by setting the resistivity between stations TT and MC at depths of 15 to 30 km to 100 Ωm, a value similar to the resistivities to the north and south of this zone. Inversion parameters were set to be the same as those for the initial model. A forward model of this structure was run and produced an rms of 5.65, considerably larger than the rms of the original model. However this model was then allowed to invert, testing whether the input features would remain upon inversion or whether the original modelled features would return. The resulting model is shown in Figure 18. This model inverted to an rms of 3.47, which is a significantly better data fit that the original model.

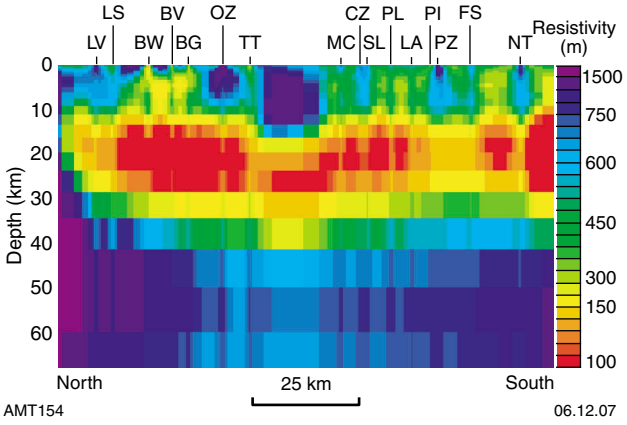

Figure 18. Results of a model run to test the depth extent of conductive features A and B, and the existence of feature C from Figure 17. Starting from the model shown in Figure 17, the top 15 km of the model space was set to a resistivity of 500 m, The model space below 30 km depth was set to 700 m and feature C between 15 km and 30 km was set to 100 m. After inversion, these input features were broadly retained. The model inverted to an rms of 3.47

Many of the detailed features in the uppermost 5 km have been remodelled, suggesting that they may be real features required by the data. Even so, features such as the vertical banding below stations NT and PZ, which are constrained by only a few data points from an individual station, should be treated with caution. However, features such as the extension toward the surface of the more conductive region below stations BW, BV, and BG, which is constrained by data from several stations, are probably real. There is no discernable difference between the depth to the top of features A and B in the original model (Fig. 17), or in the depth extent of features A and B. The resistive feature C has not been remodelled. Instead, a zone of enhanced conductivity less than 150 Ωm is relatively continuous along the model between a depth of approximately 15 km and 30 km. This result suggests that no distinction between the depths of feature A and feature B can be robustly interpreted from this model. This result suggests that no electrical distinction can be made between the crust of the northern Gascoyne Complex and the Glenburgh Terrane. The two regions may have different geological backgrounds and by coincidence share the same electrical characteristics, or instead they may be a contiguous piece of crust, with the Glenburgh Terrane forming basement to the northern Gascoyne Province.

2D induction arrow inversion

Although MT data collection was unsuccessful at numerous stations along the profile, due either to disconnection of electrodes or to severe distortion of the electric fields (particularly in the Bangemall Supergroup), the vertical magnetic field was successfully recorded at most stations and good quality induction arrow data exists along the profile. The induction arrow itself can be modelled without incorporating any electric data, so a 2D model was run of the induction arrow data along the entire profile. Two important facts should be remembered in the discussion and interpretation of this model:

1. the induction arrow model contains inherently less data than the MT model and features are therefore less well constrained, and
2. this model crosses the southern end of the profile, which has been found to have 3D effects, and the northern end of the profile where the dimensionality analysis was unreliable due to severe distortion. Induction arrows are less sensitive to many 3D effects than MT data because current gathering, where charges accumulate at the boundaries of resistivity domains (Wannamaker et al., 1984), does not affect the magnetic field and also because the vertical magnetic field integrates data over a larger volume than the electric field (Simpson and Bahr, 2005). However, caution should still be exercised when interpreting the model since out-of-plane features may be modelled in the plane of the profile. The best test for the existence of these features is through further 3D forward modelling.

Inversion results

A 2D inversion was run from a starting half-space of 100 Ωm. Tau was set to 3 and the error floor on all induction arrow data was set to 0.05. The profile line was perpendicular to the geoelectric strike determined from the phase tensor analysis, at 120°. This direction is also approximately perpendicular to the direction of many of the induction arrows, particularly at periods greater than approximately 200 s.

The model inverted to an rms of 3.08 and is shown in Figure 19. For clarity, this model and subsequent models of induction arrow data are shown with a vertical exaggeration of approximately 1.6. Several features of note have been modelled. *Feature A* is a zone of lower resistivity in the uppermost approximately 15 km that extends approximately from station LV to station NT. This feature probably corresponds to the low resistivity feature modelled at this location in the 2D MT model. Testing of that model showed that no changes in its depth extent along its length were required by the data. South of approximately station NT, this lower resistivity zone appears to dip to the south and extend to depths between approximately 20 and 40 km (*Feature B*). It is truncated to the south by the higher resistivity *Feature C,* which outcrops from station NM south and extends to a depth of approximately 20 km. The higher resistivity *Feature D* lies below Features A and B and extends to the surface in the ~25 km long gap between stations MT and LV. As noted previously, the NLCG modelling program often models resistive bodies where there are larger gaps between stations, so this extension to the surface may not be required by the data.

Feature E is a lower resistivity zone between approximately station CS and MT. It has quite a variable depth extent, in some places reaching the surface and in others beginning at approximately 10 km depth and extending to depths of between 10 km and approximately 90 km. At these large depths the feature is modelled as quite a diffuse body and

they may represent smoothing downwards of a shallower (e.g. 50 km deep) feature. To the north, Feature E is truncated by the higher resistivity *Feature F* along a steeply-dipping boundary that appears to extend to the base of the model. Feature F extends from approximately 2 km depth beneath stations CY, NA, and NB.

As shown on Figure 19, many of the modelled features correspond closely with outcropping geological regions. Specifically, Feature A corresponds with much of the Gascoyne Complex. Feature D, which may be partly spurious, truncates it in a region where there is no data, but it could otherwise conceivably match up with the conductor in the uppermost 15 km beneath stations SU and MT, thus reaching across the entire Gascoyne Complex. Feature C corresponds in outcrop with the northern Yilgarn Craton. If these correlations are correct, the existence of Feature B would suggest that the margin between the Glenburgh Terrane and the Yilgarn Craton is south-dipping and that the southern Glenburgh Terrane is wedged beneath the northern Yilgarn Craton. While it is not possible to know the southerly outcrop extent of the Pilbara Craton as it is obscured by the Bangemall Supergroup, its approximate location is probably similar to the extent of the resistive feature F. It is possible that the less resistive feature E is related to a structure separating the Gascoyne Complex from the Pilbara Craton.

Model tests

If Feature B does represent crust of the Glenburgh Terrane that is wedged beneath the Yilgarn Craton, it is a significant result in terms of understanding the geometry of the Capricorn Orogen. Therefore, a model was run to test for the dip of Feature B. Beginning with the model shown in Figure 19, a boundary was made from station NM at the surface, dipping north at approximately 45°. Cells to the north of and below this boundary were set to a resistivity of 1850 m, as shown in Figure 20. This effectively removed Feature B and set the boundary between Feature A and Feature C to be north-dipping. A forward model run from this starting model with the same parameters as described above had an rms of 3.523. Although the rms error of the whole model is only slightly higher than that of the initial model, the rms errors of the individual stations affected by the model test have increased dramatically, as shown in Figure 21. When allowed to invert, this model inverted to an rms of 3.09, which is very similar to the initial model rms of 3.08. The inverted model is shown in Figure 22. This shows that the original dip on this boundary has been recovered. Individual stations' rms errors have also decreased to similar values as the initial model (Fig. 21), providing additional support that the data require a south-dipping feature (*Feature B*). However, due to the reasons outlined above, this feature, together with the other important features imaged in this model, should be tested by 3D forward modelling.

3D forward modelling

3D forward modelling is the most robust and reliable modelling technique for a region such as this, which has geoelectrically 3D regions and also regions of severe distortion of MT data. 3D forward modelling involves setting up a 3D resistivity grid and determining what data that resistivity structure would produce. These synthetic data are then compared with the station data to determine what differences exist between the measured earth and the input resistivity grid. Forward modelling is therefore particularly useful for hypothesis testing, where a hypothesized resistivity structure can be input into the grid and the resulting data compared with the station data. Since the induction arrow data are of good quality along the whole profile and are unaffected by small-scale, local structures, they will be used for comparisons with the 3D forward modelled data.

3D forward modelling was carried out using Mackie's MTD3FWD code (Mackie and Madden, 1993; Mackie et al., 1993) contained in the WinGLink software package.

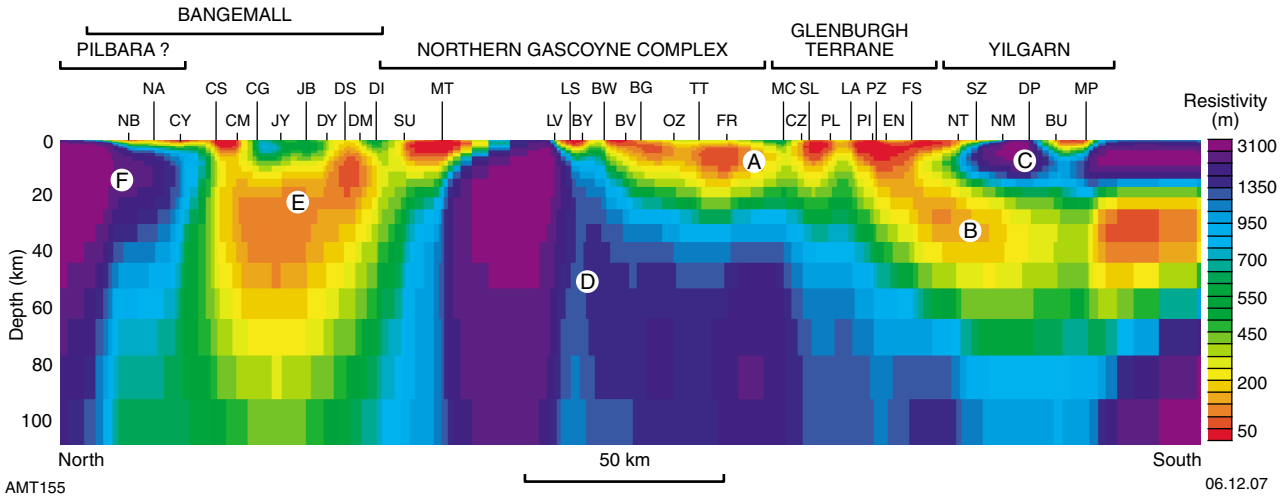

Figure 19. 2D model of induction arrow data from the whole profile, showing the approximate location of the major outcropping geological regions along the profile line. This model inverted to an rms of 3.08. Low resistivity features A, B, and E and high resistivity features C, D, and F were modelled

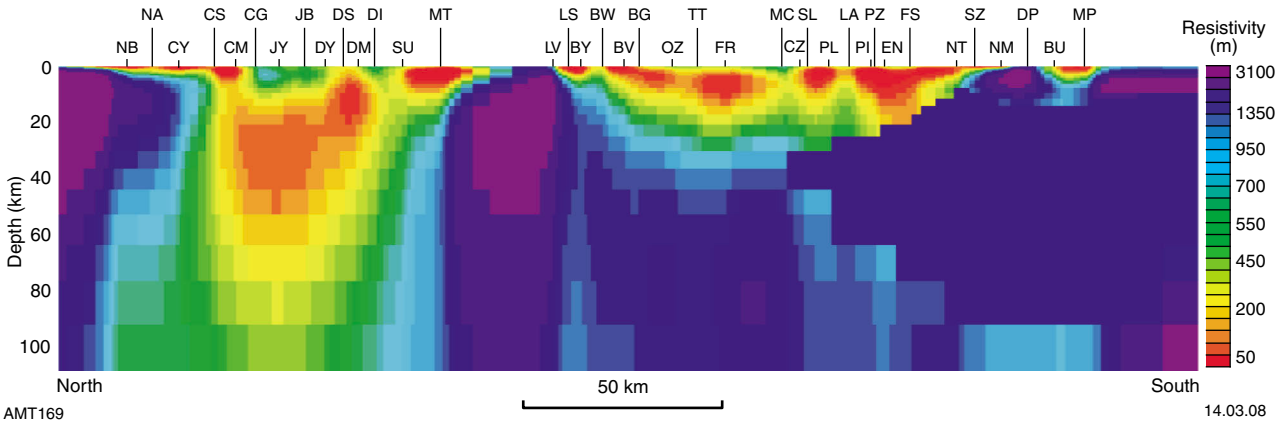

Figure 20. 2D induction arrow model that was conducted to test for the dip of feature B, interpreted to represent the Errabiddy Shear Zone. A low resistivity region was input into the model that starts at station NM at the surface and dips north at approximately 45°. Cells to the north of and below this boundary were set to a resistivity of 1850 m. A forward model produced an rms of 3.523

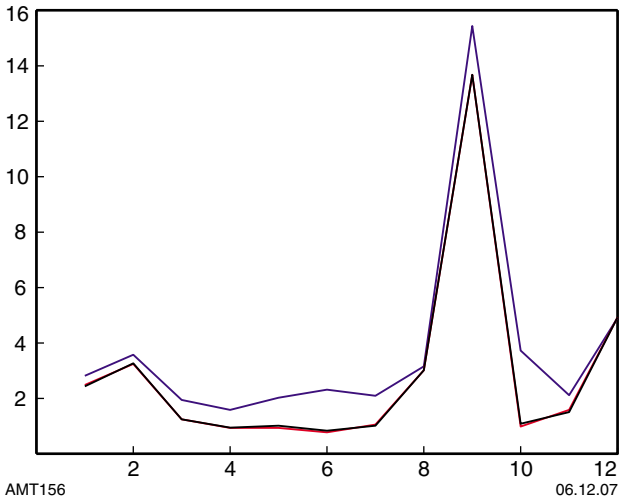

Figure 21. RMS errors for stations PL to MP that are affected by a model test shown in Figure 20. The black line shows the errors for the initial model (Fig. 19). The blue line shows the errors for the forward model (Fig. 20). The red line shows the errors for the inverted test model

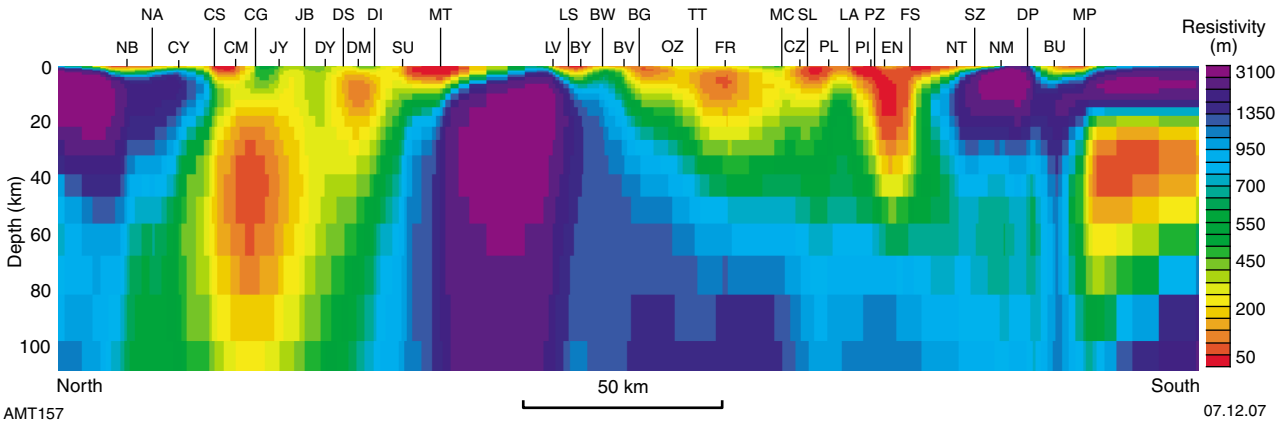

Figure 22. 2D induction arrow model produced by inverting the model shown in Figure 20. This model inverted to an rms of 3.08

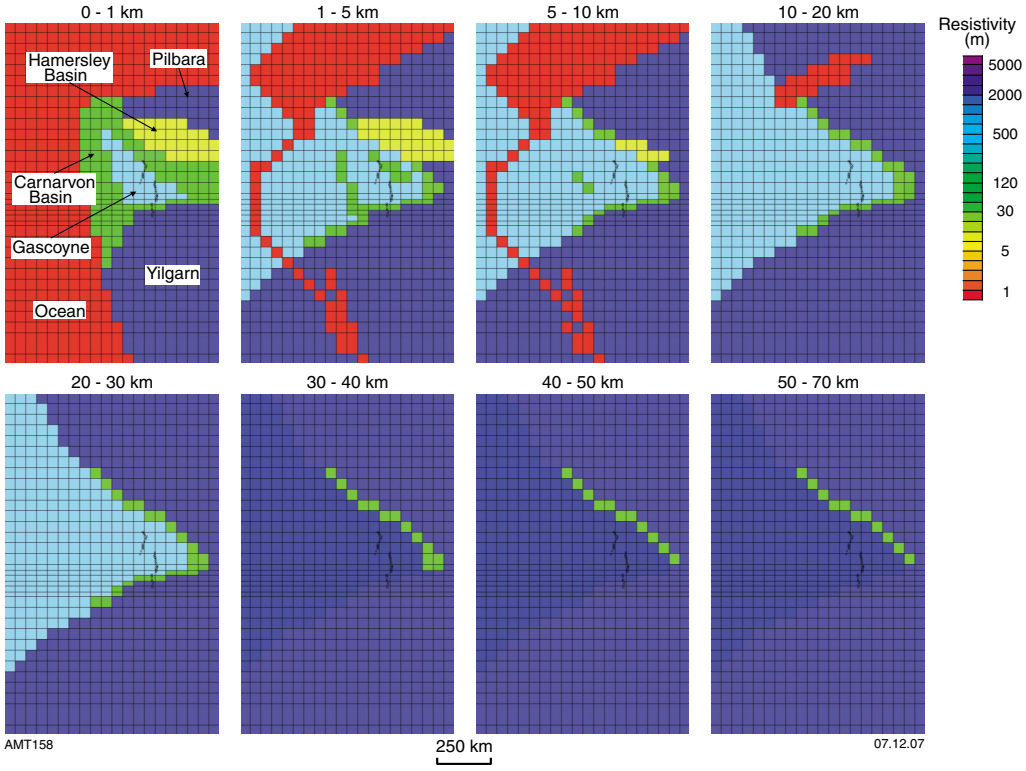

Figure 23. Initial resistivity mesh. The mesh is shown as 6 depth layers. The crosses toward the centre of the mesh show the locations of the MT stations

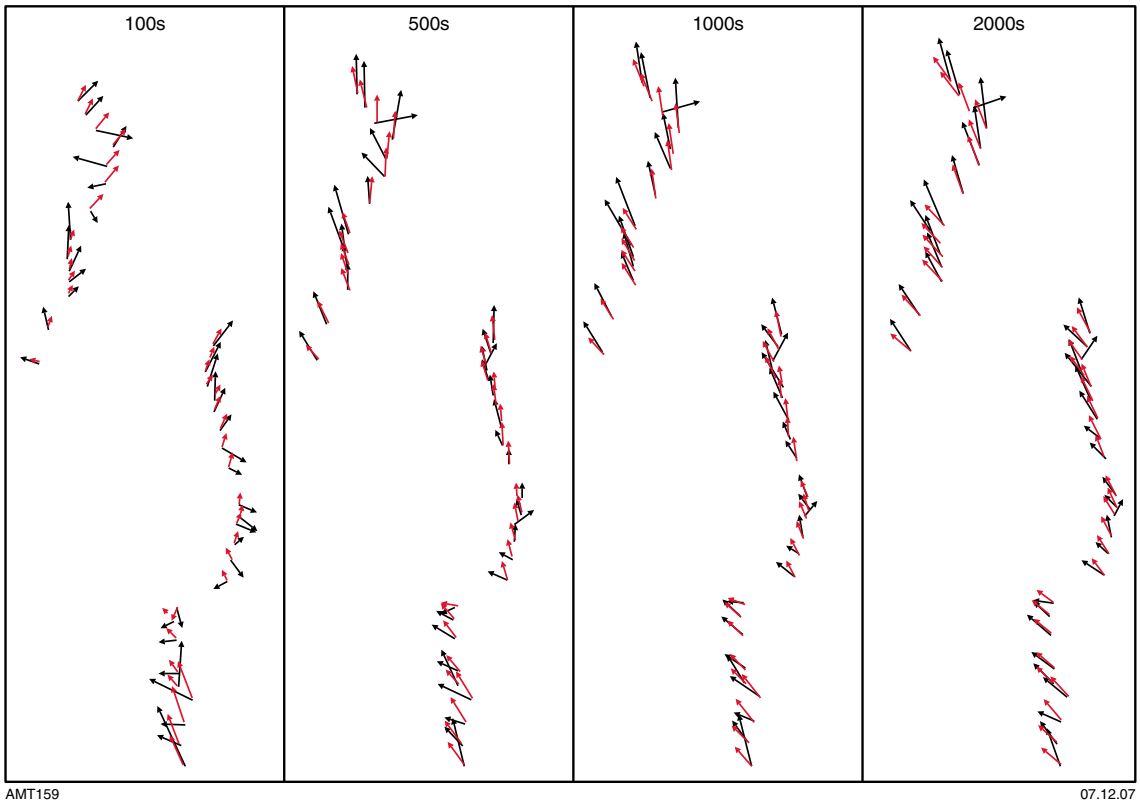

Figure 24. Comparison of induction arrows produced by running a 3D forward model of the initial resistivity mesh (red) with the station data (black) at 100 s, 500 s, 1000 s, and 2000 s

Initial models were set up that measured approximately 450 km north–south, 300 km east–west, and 70 km deep. The synthetic induction arrows these models produced were significantly different to the station data and at long periods pointed strongly to the west. Therefore much larger grids were set up, measuring 1600 km north–south, 1000 km east–west, and 70 km deep. The coastline, ocean, and sedimentary basins both in the ocean and on the continent were input into the grid. The depths of the sedimentary basins were taken from the SEEBASE™ dataset. A forward model derived from a simple combination of the geological features seen at the surface with the resistivity features modelled in the 2D MT model and the 2D induction arrow model, extrapolated with depth, was run. The horizontal layers of the model are shown in Figure 23. The specific geological or resistivity regions being forward modelled are marked on the figure. Archean cratons throughout the world have often been found to be more resistive than Proterozoic or younger terranes (e.g. Jones et al., 2005b) and the regions interpreted to represent the Yilgarn and Pilbara Cratons on the 2D induction arrow model (Fig. 19) are highly resistive, so the expected locations of the Pilbara and Yilgarn Cratons were forward modelled with a resistivity of 4200 Ωm. The expected location of the Gascoyne Complex was forward modelled with a more moderate resistivity of 500 Ωm, which increases to a resistivity of 2000 Ωm below 30 km depth as expected from both the 2D MT model (Fig. 17) and the 2D induction arrow model (Fig. 19). The 2D induction arrow model showed more conductive regions at the margins between interpreted Gascoyne Complex and Pilbara Craton, and interpreted Glenburgh Terrane and Yilgarn Craton. Bands along these expected margins were therefore forward modelled with a resistivity of between 23 and 34 Ωm. Seawater, oceanic sedimentary basins and continental sedimentary basins were forward modelled with low resistivities between 1 and 50 Ωm.

The synthetic induction arrows produced by this forward model at periods 100 s, 500 s, 100 s, and 2000 s are shown in red on Figure 24, overlain on the station data in black. The forward model has reproduced most of the major trends in the induction arrows well, particularly at periods 1000 s and 2000 s where the directions and magnitudes of the induction arrows have been quite closely reproduced. The most significant differences occur between the 100 s arrows, where almost all of the synthetic arrows point in a more northerly direction than the station data, which point more westerly in the southern end of the line and more easterly throughout most of the Gascoyne Complex and the Bangemall Supergroup. Some of the variations seen in the station data at a period of 100 s are most likely due to smaller-scale local structures which are too detailed to include in the forward model mesh.

Once this 3D mesh was found to be a relatively good match for the station data, it was used as a base for hypothesis testing of other possible lithospheric architectures. The first such test was the location of the boundary between the Gascoyne Complex and the Pilbara Craton. The precise location of this boundary is not known as it is hidden by the Bangemall Supergroup, but it has been proposed that major structures such as the Wanna Syncline and Talga Fault that controlled sedimentation into the Bangemall Supergroup may be related to this boundary (Fig. 1; Martin and Thorne, 2004). In the initial model mesh described above, the boundary was placed in the approximate location of the Talga Fault. A 3D forward model was run with the same parameters as the initial forward model but the boundary between the Pilbara Craton and the Gascoyne Complex placed slightly further south, correlating to the location of the Wanna Syncline. The model mesh is shown in Figure 25 and the synthetic induction arrows produced by the forward model at periods 100 s, 500 s, 100 s, and 2000 s are shown in red on Figure 26, overlain on the station data in black. At all displayed periods, but particularly 100 s, 500 s, and 1000 s, the synthetic arrows at the northern end of the profile do not fit the station data as well as the synthetic arrows from the initial forward model do. These data therefore suggest that a more northerly electrical boundary exists.

The 2D induction arrow model produced a broad low resistivity feature beneath much of the Bangemall Supergroup (Fig. 19), which was interpreted to possibly represent the boundary between the Pilbara Craton and the Gascoyne Complex. Therefore, to further test for the location of this boundary, a second 3D forward model test was run. In this model a broader region of lower resistivity encompassing both the location of the Talga Fault (from the initial model) and the Wanna Syncline (from the model test described above) was input into the forward model mesh. This model mesh is shown in Figure 27 and the synthetic induction arrows produced by the forward model at periods 100 s, 500 s, 100 s, and 2000 s are shown in red on Figure 28, overlain on the station data in black. The synthetic arrows at 100 s period fit the station data very closely in the Bangemall Supergroup and the northern Gascoyne Complex. However, at longer periods, the synthetic arrows do not fit the data any more closely than those of the initial forward model did and generally point approximately 30° clockwise from the station data. This result suggests that there may be a broader conductive region at shallower depths in this region (corresponding to a period of 100 s), but the data do not support this broader conductive region extending to depth. This has therefore been a useful test of the results of the 2D induction arrow model. The broad, deep conductive region seen in that model may be partly due to out-of-plane 3D features, or it may be due to a smoothing downwards of a shallower feature.

The boundary between the Glenburgh Terrane and the Yilgarn Craton in the initial 3D forward model (Fig. 23) is a vertical feature. However, different geological models have suggested that this boundary dips either north or south (e.g. Sheppard et al., 2004; Tyler and Thorne, 1990) and the 2D induction arrow model (Fig. 19) suggested that this boundary has a southerly dip. A forward model was therefore run to test whether a southerly dip on this boundary would fit the station data better than the current steep dip. The boundary was input into the forward model with an approximately 45° southerly dip, as shown on Figure 29. The enhanced conductivity along the boundary was input to extend to 30 km depth, as suggested by the 2D induction arrow model. The synthetic induction arrows produced by the forward model at periods 100 s, 500 s, 1000 s, and 2000 s are shown in red on Figure 30,

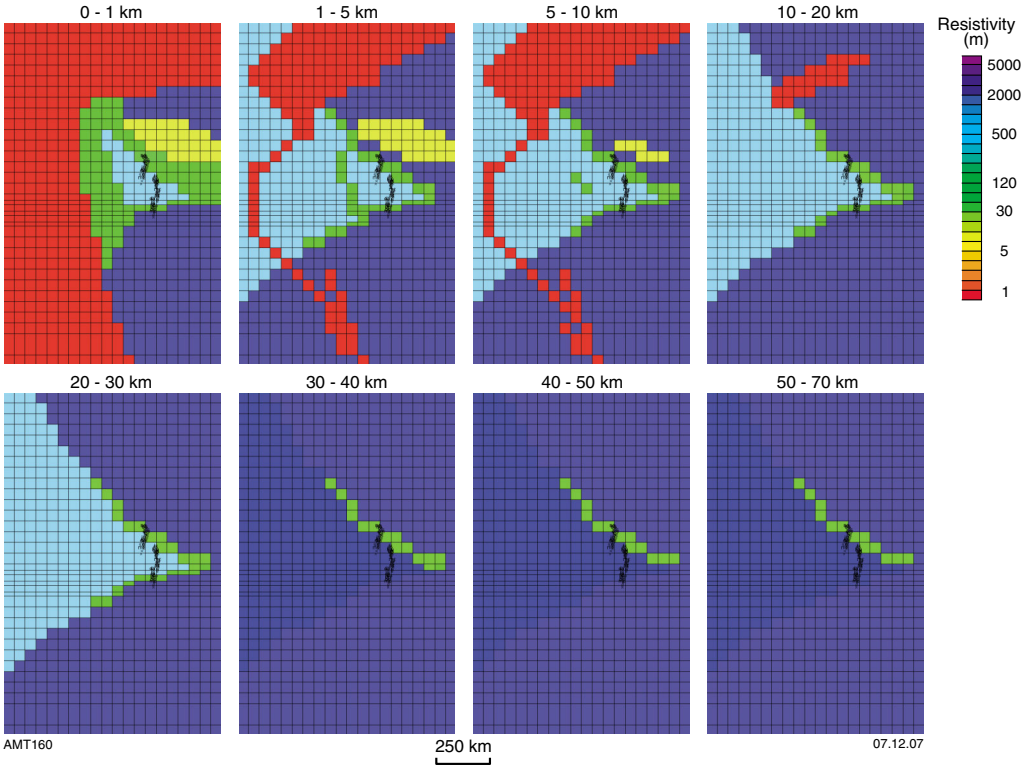

Figure 25. Resistivity mesh altered from the original (Fig. 23) by moving the boundary between the high resistivity region in the north, representing the Pilbara Craton, and the moderate resistivity region in the centre, representing the Gascoyne Complex, south. The mesh is shown as 6 depth layers. The crosses toward the centre of the mesh show the locations of the MT stations

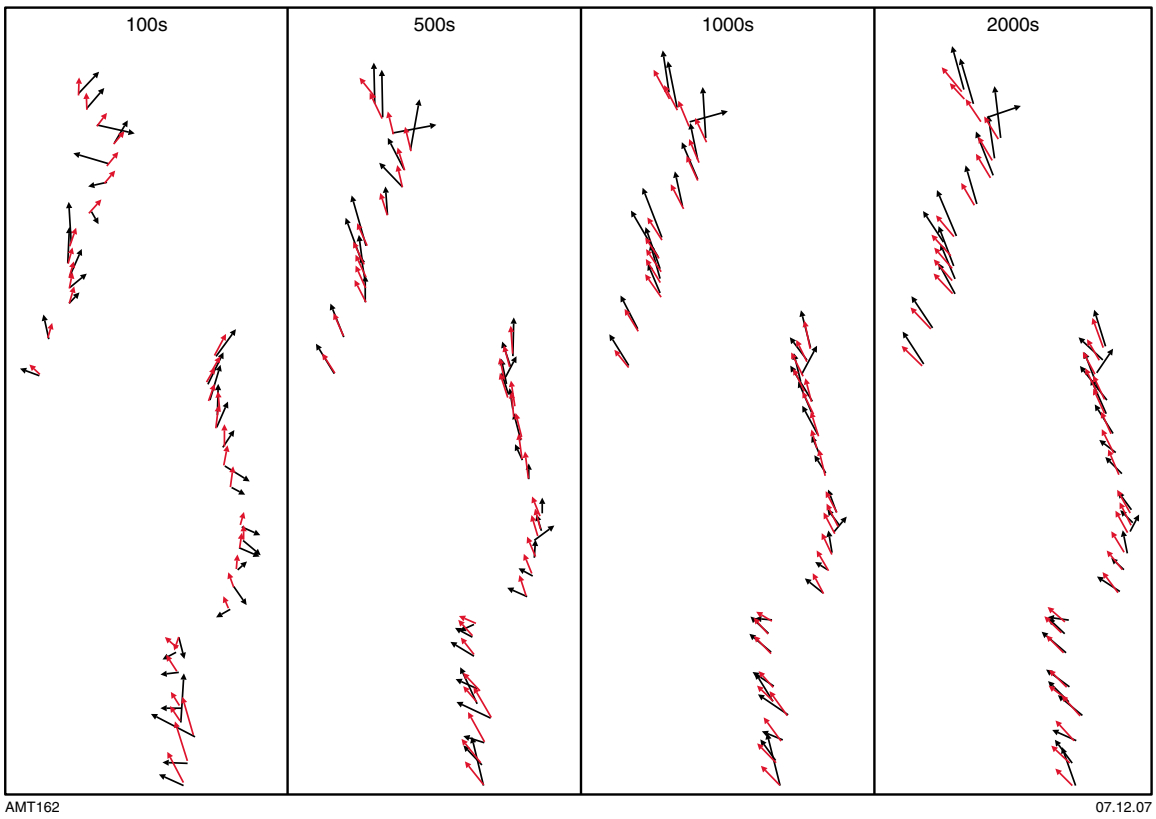

Figure 26. Comparison of induction arrows produced by running a 3D forward model of the resistivity mesh shown in Figure 25 (red) with the station data (black) at 100 s, 500 s, 1000 s, and 2000 s

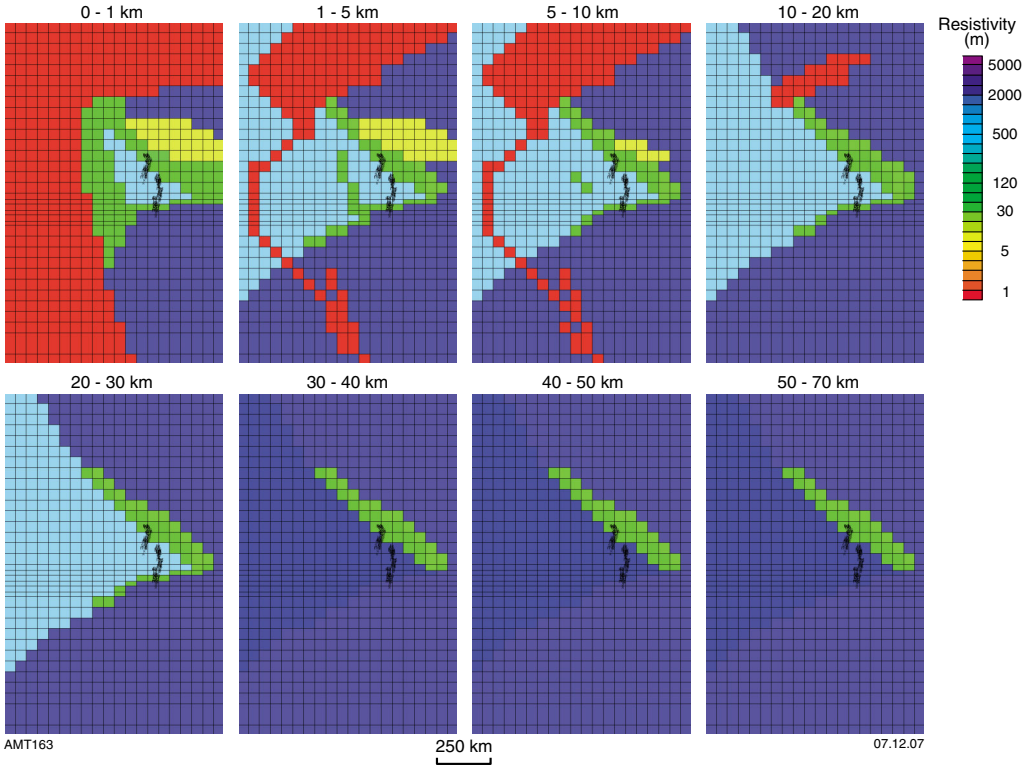

Figure 27. Resistivity mesh altered from the original (Fig. 23) by broadening the low resistivity region between the high resistivity region in the north that represents the Pilbara Craton and the moderate resistivity region in the centre that represents the Gascoyne Complex. The mesh is shown as 6 depth layers. The crosses toward the centre of the mesh show the locations of the MT stations

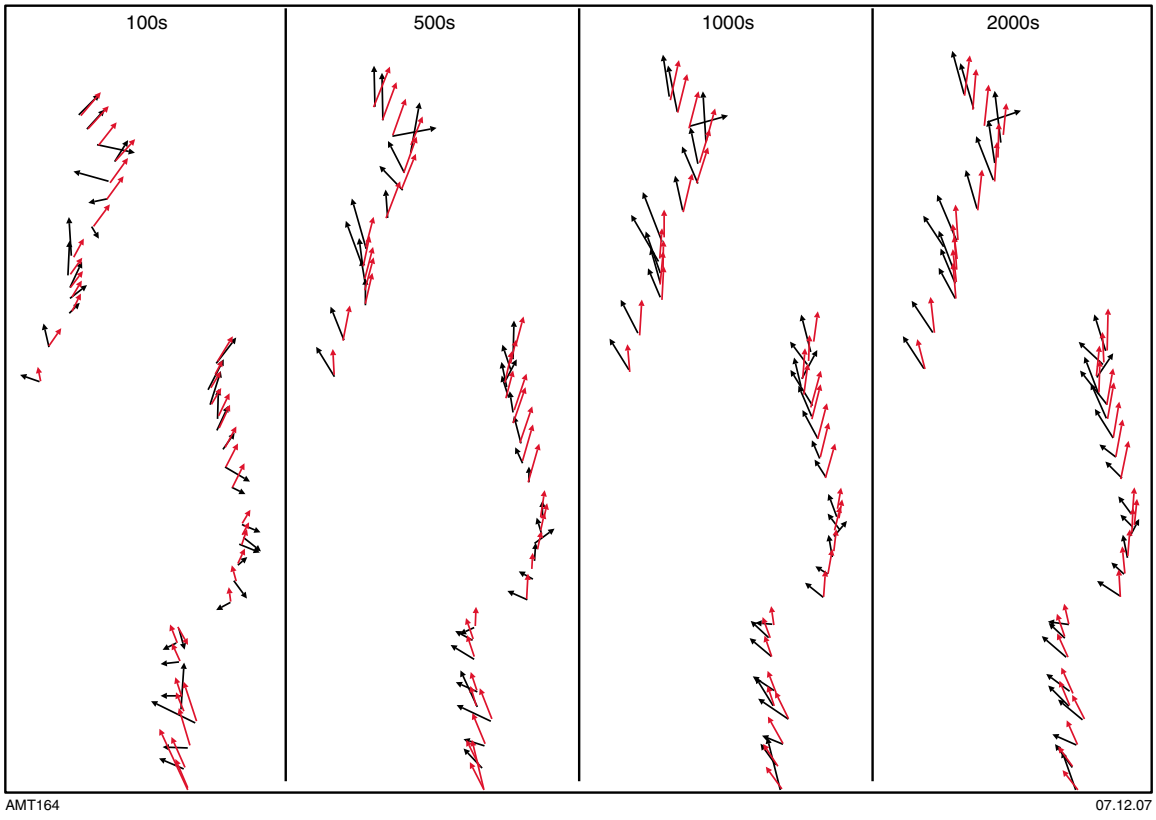

Figure 28. Comparison of induction arrows produced by running a 3D forward model of the resistivity mesh shown in Figure 27 (red) with the station data (black) at 100 s, 500 s, 1000 s, and 2000 s

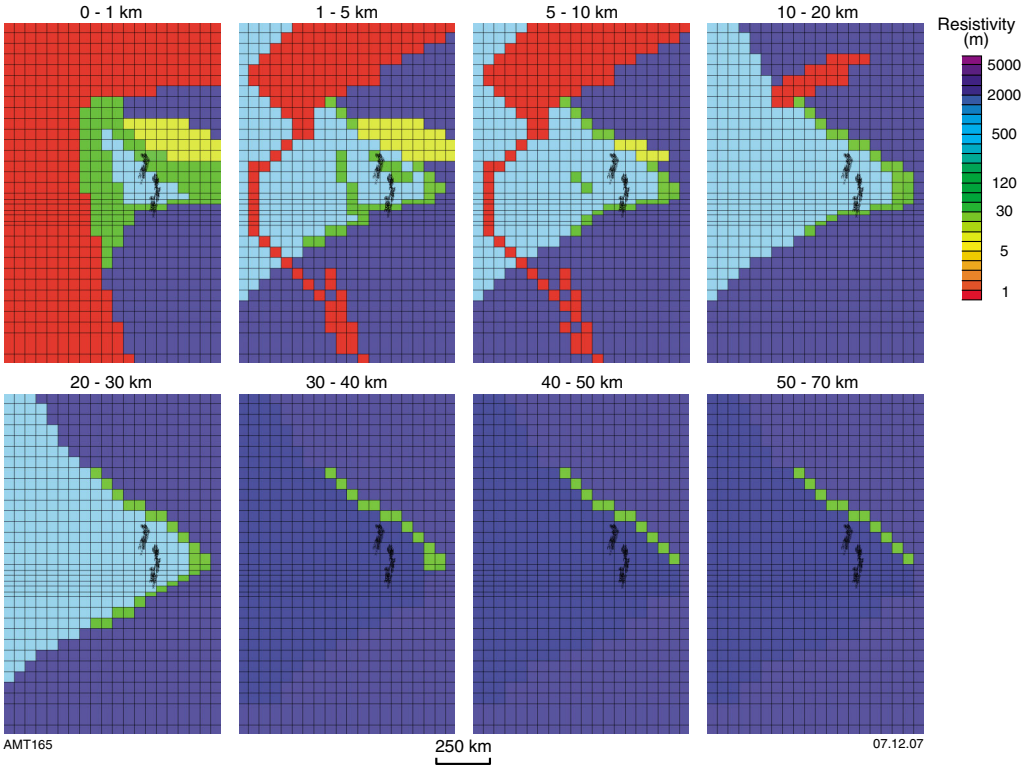

Figure 29. Resistivity mesh altered from the original (Fig. 23) by dipping the margin between the region of moderate resistivity in the centre that represents the Gascoyne Complex and the region of high resistivity in the south that represents the Yilgarn Craton south at approximately 45°

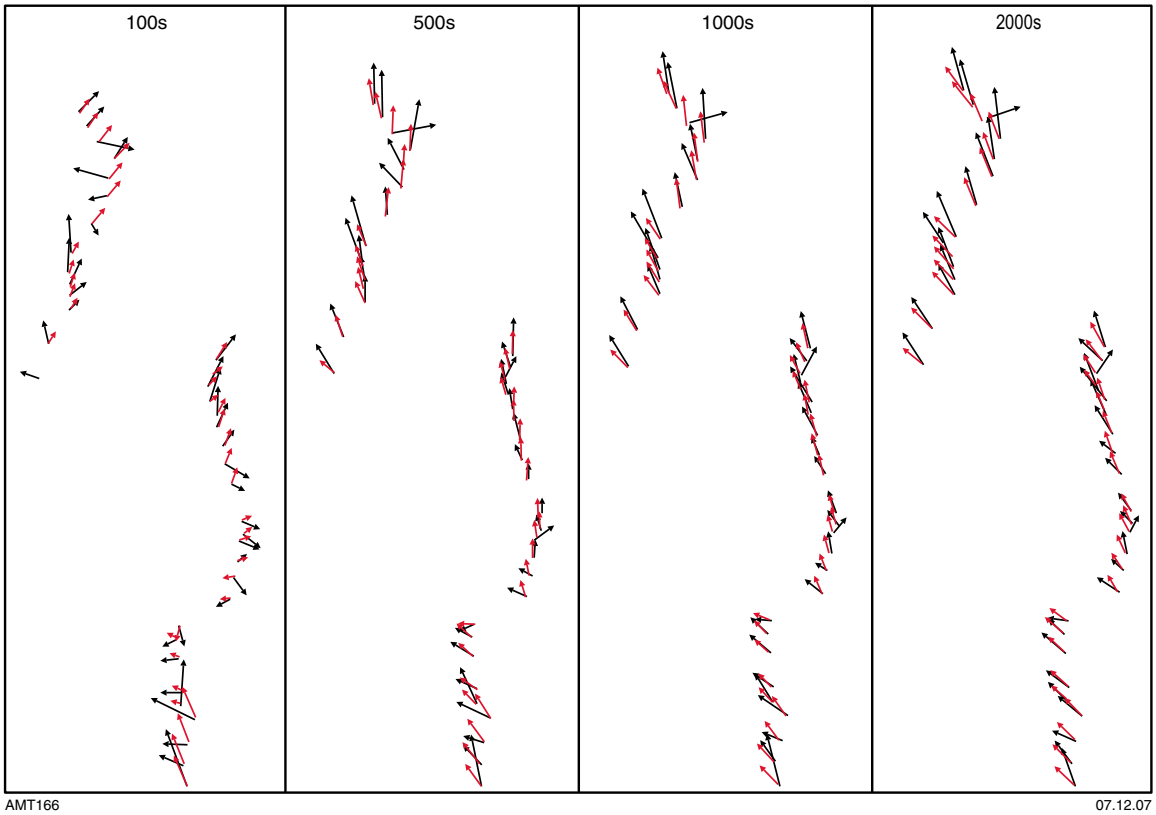

Figure 30. Comparison of induction arrows produced by running a 3D forward model of the resistivity mesh shown in Figure 29 (red) with the station data (black) at 100 s, 500 s, 1000 s, and 2000 s

overlain on the station data in black. The fit of these data to the station data is very similar to that of the initial model (Fig. 24). The main difference is seen at 100 s in the Yilgarn Craton and southern Gascoyne Complex. In this region, the induction arrows from this model fit the station data better than the initial model, with directions closer to those of the station data. At longer periods, the fit to the station data at these locations remains very good. This model therefore supports that the conductivity boundary at this location has a southerly dip.

Numerous other model tests were run which will not be displayed here because they did not make significant changes to the resulting induction arrows. However two tests are of note: in the first, the uppermost 40 km of the model was the same as the initial model, but below this the entire model space was set to a resistivity of 4200 Ωm to test for an electrically homogenous mantle. Within the error bounds and the smoothness of the induction arrow data, the differences in crustal thickness between 32 and 44 km determined by seismics (Drummond, 1981; Reading et al., 2007) will not affect the results and a single depth of 40 km will suffice. The resulting induction arrows are very similar to those of the initial model, but at periods greater than 500 s they point approximately 10° anticlockwise from the initial model, particularly in the northern half of the profile. Since this is a worse fit to the station data, this result suggests that the mantle is not electrically homogenous, supporting the result of the seismic data, but also shows that the arrows are responding much more strongly to crustal structure than mantle structure. In the second test, the Yilgarn Craton was cut off along a boundary running along an approximate longitude of 115° since this appears to be the extent of the craton from surface geology. Mesh space to the west of this boundary was set to correspond to the moderate resistivity of the Gascoyne Complex. The induction arrows produced by this forward model were indistinguishable from those of the initial model, showing that this region is too far away from the profile location for this change in resistivity to affect the recorded induction arrows.

Synthesis

An approximately 300 km long 2D MT survey was carried out in the Gascoyne region of Western Australia in September 2006. Data were collected at 57 stations, but due to problems with new instrumentation, only 39 of these stations produced data that were useful in further interpretation. The survey began in the Yilgarn Craton in the south and crossed the Glenburgh Terrane and the northern Gascoyne Complex to finish in the Bangemall Supergroup in the north. The survey was run primarily to investigate the lithospheric architecture of the region in order to provide constraints on several areas of geological investigation, namely:

1. the location and nature of the boundary between the Glenburgh Terrane and the Yilgarn Craton;
2. the possible existence of a major tectonic boundary between the Glenburgh Terrane and the northern Gascoyne Complex; and
3. the location and nature of the boundary between the northern Gascoyne Complex and the Pilbara Craton.

Before MT data can be utilized to address geological questions, they must undergo detailed geophysical analysis. During this analysis, two factors of the survey region were found to have a strong impact on the data. Firstly, the Bangemall region has significant topographic complexity and is crossed by many strike ridges and riverbeds, features that can often distort electrical fields and currents. This was found to be the case in this survey and most of the MT data from the Bangemall region was too distorted to be used in analysis or modelling. However, the vertical magnetic field is not affected by such distortion and good quality induction arrows were still produced by stations over the Bangemall Supergroup. Secondly, dimensionality analysis showed that the subsurface below the Yilgarn Craton is electrically 3D. Two-dimensionality increases northwards into the Gascoyne Complex but the data appear to become more 3-dimensional again in the Bangemall Supergroup, although it is difficult to know if this is simply a result of poor data quality due to the distortion. Two dimensional MT models can only be run from data that is responding to a 2D subsurface, so the 3-dimensionality of much of the data has limited 2D modelling to data from within the Gascoyne Complex.

After testing, results of 2D inversion showed that the simplest and smoothest model that could fit the data was a three-layer model (Fig. 18), with an upper layer of approximately 10 km depth and a resistivity that varies between approximately 150 and 500 Ωm; a middle layer extending between approximately 10 and 30 km and a resistivity of approximately 100 Ωm; and a lower layer with resistivity more than 500 Ωm that extends to the base of the model (60 km). No strong evidence was found for an electrical boundary or a major electrical difference between the Glenburgh Terrane and the northern Gascoyne Complex. This result does not prove that a major tectonic boundary between these two elements does not exist; the two pieces of crust could be unrelated, but coincidentally have the same electrical characteristics and therefore electrically appear to be continuous. Alternatively, this electrical character could have been imposed on the crust after the amalgamation of the Glenburgh Terrane and the northern Gascoyne Complex, obliterating their previous, and possibly contrasting, electrical characteristics. However, the strong continuity of electrical character across the region suggests that it is quite likely that the Glenburgh Terrane and the northern Gascoyne Complex are a contiguous piece of crust, with the older Glenburgh Terrane forming basement to the northern Gascoyne Complex. This interpretation suggests that the resistivity layers would be at a greater depth beneath the northern Gascoyne Complex than the Glenburgh Terrane, but testing of the model showed that the data cannot determine whether such a depth offset is present.

2D inversions of induction arrow data from the whole profile were run with the aim of investigating the electrical nature of the boundaries between the Pilbara Craton, Gascoyne Complex and Yilgarn Craton, that had not been possible with the 2D MT model. Although the induction arrow data do not suffer from distortion and can be less strongly affected by 3D features than MT data, the models should be interpreted with caution since 3D bodies can still lead to spurious model features. A

significant boundary was modelled between the Glenburgh Terrane and the Yilgarn Craton, with the less resistive Glenburgh Terrane appearing to dip south beneath the Yilgarn Craton (Fig. 19). Model tests show that the data require this boundary to be south-dipping (Figs 20–22). A significant boundary was also modelled between the interpreted northern Gascoyne Complex and the Pilbara Craton, corresponding in location to the Wanna Syncline (Fig. 19). This boundary separates more resistive crust to the north from a broad region of low resistivity that extends to mantle depths beneath the Bangemall Supergroup.

Hypotheses about the lithospheric structure of the region and the specific features modelled in the 2D inversions of induction arrow data were tested through 3D forward modelling. Numerous possible architectures were tested, with the following features best fitting the station data:

- the ocean, oceanic basins, and continental basins have a low resistivity (Figs 23 and 24);
- the Pilbara and Yilgarn Cratons have a high resistivity, whereas the Gascoyne Complex has a moderate resistivity to 30 km depth that increases to a higher resistivity at greater depths (Figs 23 and 24);
- the boundaries between the Gascoyne Complex and the Yilgarn and Pilbara Cratons are marked by bands of low resistivity, at least to crustal depths (Figs 23and 24);
- the boundary between the Gascoyne Complex and the Yilgarn Craton (marked by the Errabiddy Shear Zone) dips south, and crust of the Glenburgh Terrane is wedged beneath the northern Yilgarn Craton (Figs 29 and 30) . This supports the interpretations of Sheppard et al. (2004); and
- the location of the boundary between the Gascoyne Complex and Pilbara Craton is approximately that of the Talga Fault, just to the north of the MT survey line (Figs 23 to 26). A broader, low resistivity region extends to the Wanna Syncline at shallower depths (Figs 27 and 28).

References

Bahr, K, 1988, Interpretation of the magnetotelluric impedance tensor: regional induction and local telluric distortion: Journal of Geophysics, v. 62, p. 119–127.

Bibby, HM, Caldwell, TG, and Brown, C, 2005, Determinable and non-determinable parameters of galvanic distortion in magnetotellurics: Geophysical Journal International, v. 163(3). p. 915–930.

Cagniard, L, 1953, Basic theory of the magnetotelluric method of geophysical prospecting: Geophysics, v. 18, p. 605–645.

Caldwell, TG, Bibby, HM, and Brown, C, 2004, The magnetotelluric phase tensor: Geophysical Journal International, v. 158(2), p. 457–469.

Cantwell, T, 1960, Detection and analysis of low-frequency magnetotelluric signals: M.I.T., Cambridge, Mass.,PhD thesis.

Cawood, PA, and Tyler, IM, 2004., Assembling and reactivating the Proterozoic Capricorn Orogen: lithotectonic elements, orogenies, and significance: Precambrian Research, v. 128, p. 201–218.

Chave, AD, and Thompson, DJ, 1989, Some comments on magnetotelluric response function estimation: Journal of Geophysical Research-Solid Earth, v. 94, p. 14215–14225.

Chave, AD, Thompson, DJ, and Ander, ME, 1987, On the robust estimation of power spectra, coherences and transfer functions: Journal of Geophysical Research-Solid Earth, v. 92, p. 633–648.

de Groot-Hedlin, C, and Constable, S, 1990, Occam Inversion to Generate Smooth, 2-Dimensional Models from Magnetotelluric Data: Geophysics, v. 55(12), p. 1613–1624.

Drummond, BJ, 1981, Crustal structure of the Precambrian terrains of northwest Australia from seismic refraction data: BMR Journal of Australian Geology and Geophysics, v. 6, p. 123–135.

Duba, A, Heikamp, S, Meurer, W, Nover, G, and Will, G, 1994, Evidence from Borehole Samples for the Role of Accessory Minerals in Lower-Crustal Conductivity: Nature, v. 367(6458), p. 59–61.

Duba, A, Huenges, E, Nover, G, Will, G, and Jödicke, H, 1988, Impedance of Black Shale from Munsterland-1 Borehole — an Anomalously Good Conductor: Geophysical Journal-Oxford, v. 94(3), P. 413–419.

Ferguson, IJ, Craven, JA, Kurtz, RD, Boerner, DE, Bailey, RC, Wu, X, Orellana, MR, Spratt, J, Wennberg, G, and Norton, N, 2005a, Geoelectric response of Archean lithosphere in the western Superior Province, central Canada: Physics of the Earth and Planetary Interiors, v. 150(1–3), p. 123–143.

Ferguson, IJ, Stevens, KM, and Jones, AG, 2005b, Electrical-resistivity imaging of the central Trans-Hudson orogen: Canadian Journal of Earth Sciences, v. 42(4), p. 495–515.

Frost, BR, Fyfe, WS, Tazaki, K, and Chan, T, 1989, Grain-Boundary Graphite in Rocks and Implications for High Electrical-Conductivity in the Lower Crust: Nature, v. 340(6229), p. 134–136.

Gamble, TD, Clarke, J, and Goubau, WM, 1979a, Magnetotellurics with a Remote Magnetic Reference: Geophysics, v. 44(1), p. 53–68.

Gamble, TD, Goubau, WM, and Clarke, J, 1979b, Error Analysis for Remote Reference Magnetotellurics: Geophysics, v. 44(5), p. 959–968.

Gamble, TD, Goubau, WM, and Clarke, J, 1979c, Magnetotellurics with a Remote Magnetic Reference: Geophysics, v. 44(3), p. 402–402.

Garcia, X, and Jones, AG, 2005, Electromagnetic image of the Trans-Hudson orogen — THO94 transect: Canadian Journal of Earth Sciences, v. 42(4), p. 479–493.

Gee, RD, 1979, Structure and tectonic style of the Western Australian shield: Tectonophysics, v. 58, p. 327–369.

Glover, PWJ, 1996, Graphite and Electrical Conductivity in the Lower Continental Crust: A Review: Physics and Chemistry of the Earth, v. 21(4), p. 279–287.

Glover, PWJ, and Vine, FJ, 1992, Electrical-Conductivity of Carbon-Bearing Granulite at Raised Temperatures and Pressures: Nature, v. 360(6406), p. 723–726.

Glover, PWJ, and Vine, FJ, 1995, Beyond Ktb — Electrical-Conductivity of the Deep Continental-Crust: Surveys in Geophysics, v. 16(1), p. 5–36.

Groom, RW, and Bailey, RC, 1991, Analytic Investigations of the Effects of near-Surface 3-Dimensional Galvanic Scatterers on Mt Tensor Decompositions: Geophysics, v. 56(4), p. 496–518.

Hackney, R, 2004, Gravity anomalies, crustal structure and isostasy associated with the Proterozoic Capricorn Orogen, Western Australia: Precambrian Research, v. 128(3–4), p. 219–236.

Halilovic, J, Cawood, PA, Jones, JA, Pirajno, F, and Nemchin, AA, 2004, Provenance of the Earaheedy Basin: implications for assembly of the Western Australian Craton: Precambrian Research, v. 128(3–4), p. 343–366.

Hauk, V, et al., 1997, KTB and the electrical conductivity of the crust: Journal of Geophysical Research-Solid Earth, v. 102(B8), p. 18289–18305.

Heinson, G, Direen, NG, and Gill, R, 2006, Magnetotelluric evidence for a deep-crustal mineralising system beneath the giant Olympic Dam Iron-Oxide Copper Gold deposit, southern Australia: Geology, v. 34(7), p. 573–576.

Jödicke, H, Kruhl, JH, Ballhaus, C, Giese, P, and Untiedt, J, 2004, Syngenetic, thin graphite-rich horizons in lower crustal rocks from the Serre San Bruno, Calabria (Italy), and implications for the nature of high-conducting deep crustal layers: Physics and Chemistry of the Earth, v. 141, p. 37–58.

Jones, AG, 1993, Electromagnetic Images of Modern and Ancient Subduction Zones: Tectonophysics, v. 219(1–3), p. 29–45.

Jones, AG, 1999, Imaging the continental upper mantle using electromagnetic methods: Lithos, v. 48, p. 57–80.

Jones, AG, and Gough, DI, 1995, Electromagnetic images of crustal structures in southern and central Canadian Cordillera: Canadian Journal of Earth Sciences, v. 32(10), p. 1541–1563.

Jones, AG, Ledo, J, and Ferguson, IJ, 2005a, Electromagnetic images of the Trans-Hudson Orogen: The North American Central Plains anomaly revealed: Canadian Journal of Earth Sciences, v. 42(4), p. 457–478.

Jones, AG, Ledo, J, Ferguson, IJ, Farquharson, C, Garcia, X, Grant, N, McNeice, G, Roberts, B, Spratt, J, Wennbergh, G, Wolnec, L, and Xianghang, W, 2005b, The electrical resistivity structure of Archean to Tertiary lithosphere along 3200 km of SNORCLE profiles, northwestern Canada: Canadian Journal of Earth Sciences, v. 42, p. 1257–1275.

Jones, AG, Snyder, D, Hammer, S, Asudeh, I, White, D, Eaton, D, and Clarke, G, 2002, Magnetotelluric and teleseismic study across the Snowbird Tectonic Zone, Canadian Shield: A Neoarchean mantle suture?: Geophysical Research Letters, v. 29(17), p. 10–14.

Jones, FW, and Price, AT, 1970, The perturbations of alternating geomagnetic fields conductivity anomalies: Geophysical Journal of the Royal astronomical Society, v. 20, p. 317–334.

Kinny, PD, Nutman, AP, and Occhipinti, SA, 2004, Reconnaissance dating of events recorded in the southern part of the Capricorn Orogen: Precambrian Research, v. 128(3–4), p. 279–294.

Krapez, B, 1999, Stratigraphic record of an Atlantic-type global tectonic cycle in the Palaeoproterozoic Ashburton Province of Western Australia: Australian Journal of Earth Sciences, v. 46(1), p. 71–87.

Livelybrooks, D, Mareschal, M, Blais, E, and Smith, JT, 1996, Magnetotelluric delineation of the Trillabelle massive sulfide body in Sudbury, Ontario: Geophysics, v. 61(4), p. 971–986.

Luenberger, DG, 1984, Linear and nonlinear programming: Addison-Wesley Publishing Company, Reading, Massachusetts, 560p.

Mackie, RL, and Madden, TR, 1993, 3-Dimensional Magnetotelluric Inversion Using Conjugate Gradients: Geophysical Journal International, v. 115(1), p. 215–229.

Mackie, RL, Madden, TR, and Wannamaker, PE, 1993, Three-dimensional magnetotelluric modeling using difference equations-Theory and solutions: Geophysics, v. 58, p. 215–226.

Madden, TR, and Nelson, P, 1964, reprinted 1986. A defence of Cagniard's magnetotelluric method, *in* Society of Exploration Geophysicists, Geophysics reprint series *edited by* K Vozoff: Society of Exploration Geophysicists, Tulsa, Oklahoma, 763p.

Mareschal, M, Fyfe, WS, Percival, J, and Chan, T, 1992, Grain-Boundary Graphite in Kapuskasing Gneisses and Implications for Lower-Crustal Conductivity: Nature, v. 357(6380), p. 674–676.

Martin, DMcB, and Thorne, AM, 2004, Tectonic setting and basin evolution of the Bangemall Supergroup in the northwestern Capricorn Orogen: Precambrian Research, v. 128(3–4), p. 385–409.

Mathez, EA, et al., 1995, Electrical-Conductivity and Carbon in Metamorphic Rocks of the Yukon–Tanana Terrane, Alaska: Journal of Geophysical Research-Solid Earth, v. 100(B6), p. 10187–10196.

Myers, JS, 1993. Precambrian history of the West Australian Craton and adjacent orogens: Annual Review of Earth and Planetary Sciences, v. 21, p. 453–485.

Occhipinti, SA, Sheppard, S, Myers, JS, Tyler, IM, and Nelson, DR, 2001, Archaean and Palaeoproterozoic geology of the Narryer Terrane (Yilgarn Craton) and the southern Gascoyne Complex (Capricorn Orogen), Western Australia — a field guide: Geological Survey of Western Australian, Record 2001/8, 78p.

Occhipinti, SA, Sheppard, S, Nelson, DR, Myers, JS, and Tyler, IM, 1998, Syntectonic granite in the southern margin of the Palaeoproterozoic Capricorn Orogen, Western Australia: Australian Journal of Earth Sciences, v. 45(4), p. 509–512.

Occhipinti, SA, Sheppard, S, Passchier, C, Tyler, IM, and Nelson, DR, 2004, Palaeoproterozoic crustal accretion and collision in the southern Capricorn Orogen: the Glenburgh Orogeny: Precambrian Research, v. 128(3–4), p. 237–255.

Parkinson, W, 1959, Directions of rapid geomagnetic variations: Geophysical Journal of the Royal Astronomical Society, v. 2, p. 1–14.

Pirajno, F, Jones, JA, Hocking, RM, and Halilovic, J, 2004, Geology and tectonic evolution of Palaeoproterozoic basins of the eastern Capricorn Orogen, Western Australia: Precambrian Research, v. 128(3–4), p. 315–342.

Polak, E, 1971. Computational methods in optimisation: A unified approach: Academic Press, New York, 329p.

Powell, CM, Preiss, WV, Gatehouse, CG, Krapez, B, and Li, ZX, 1994, South Australian Record of a Rodinian Epicontinental Basin and Its Mid-Neoproterozoic Breakup (Similar-to-700 Ma) to Form the Palaeo-Pacific Ocean: Tectonophysics, v. 237(3–4), p. 113–140.

Rasmussen, B, Fletcher, IR, and Sheppard, S, 2005, Isotopic dating of the migration of a low-grade metamorphic front during orogenesis: Geology, v. 33(10), p. 773–776.

Reading, AM, Kennett, BLN, and Goleby, BR, 2007, New constraints on the seismic structure of West Australia: Evidence for terrane stabilization prior to the assembly of an ancient continent?: Geology, v. 35(4), p. 379–382.

Reddy, SM, and Occhipinti, SA, 2004, High-strain zone deformation in the southern Capricorn Orogen, Western Australia: kinematics and age constraints: Precambrian Research, v. 128(3–4), p. 295–314.

Rodi, W, and Mackie, RL, 2001, Nonlinear conjugate gradients algorithm for 2-D magnetotelluric inversion: Geophysics, v. 66(1), p. 174–187.

Selway, K, Heinson, G, and Hand, M, 2006,. Electrical evidence of continental accretion: Steeply-dipping crustal-scale conductivity contrast: Geophysical Research Letters, v. 33(6), L06305, doi:10.1029/2005GL025328.

Selway, K, Heinson, G, and Hand, M, 2006b, Lithospheric architecture of central Australia from magnetotellurics: Australian Earth Sciences Convention. GSA & ASEG, Mebourne, Australia, 129p.

Sheppard, S, Occhipinti, SA, and Nelson, DR, 2005, Intracontinental reworking in capricorn Orogen, Western Australia: the 1680–1620 Ma Mangaroon Orogeny: Australian Journal of Earth Sciences, v. 52(3), p. 443–460.

Sheppard, S, Occhipinti, SA, and Tyler, IM, 2001, The tectonic setting of granites in the southern Gascoyne Complex: Geological Survey of Western Australia, Record 2001/5, p. 3–4.

Sheppard, S, Occhipinti, SA, and Tyler, IM, 2003, The relationship between tectonism and composition of granitoid magmas, Yarlarweelor Gneiss Complex, Westem Australia: Lithos, v. 66(1–2), p. 133–154.

Sheppard, S, Occhipinti, SA, and Tyler, IM, 2004, A 2005–1970 Ma Andean-type batholith in the southern Gascoyne Complex, Western Australia: Precambrian Research, v. 128(3–4), p. 257–277.

Simpson, F, and Bahr, K, 2005, Practical Magnetotellurics: Cambridge University Press, Cambridge, 254p.

Sircombe, K, 2002, Reconaissance detrital zircon geochronology provenance of the Palaeoproterozoic Ashburton formation: implications for Pilbara and Yilgarn amalgamation., 16th Australian Geological Convention: Geological Society of Australia, Adelaide, p. 147.

Soyer, W, and Unsworth, MJ, 2006, Deep electrical structure of the northern Cascadia (British Columbia, Canada) subduction zone: Implications for the distribution of fluids: Geology, v. 34(1): 53-56, doi:10.1130/G21951.1.

Spratt, JE, Jones, AG, Nelson, KD, and Unsworth, MJ, 2005, Crustal structure of the India-sia collision zone, southern Tibet, from INDEPTH MT investigations: Physics of the Earth and Planetary Interiors, v. 150(1–3), p. 227–237.

Swift, CMJ, 1971, Theoretical magnetotelluric and turam response from two-dimensional inhomogeneities: Geophysics, v. 36, p. 38–52.

Telford, WM, Geldart, LP, and Sheriff, RE, 1990, Applied Geophysics: Cambridge University Press, 290p.

Thorne, AM, 1990, Ashburton Basin. Geology and mineral resources of Western Australia: Geological Survey of Western Australia, Memoir 3, p. 210–219.

Thorne, AM, and Trendall, AF, 2001, Geology of the Fortescue Group, Pilbara Craton, Western Australia: Geological Survey of Western Australia, Bulletin 144, 249p.

Tikhonov, AN, 1950, The determination of the electrical properties of the deep layers of the Earth's crust: Dokl. Acad. Nauk. SSR, v. 73, p. 295–297.

Tikhonov, AN, 1986, On determining electrical characteristics of the deep layers of the Earth's crust, *in* Magnetotelluric Methods *edited by* K Vozoff: Tulsa, Society of Exploration Geophysics, p. 2–3.

Tournerie, B, and Chouteau, M, 2005, Three-dimensional magnetotelluric survey to image structure and stratigraphy of a sedimentary basin in Hungary: Physics of the Earth and Planetary Interiors, v. 150(1–3), p. 197–212.

Tyler, IM, and Thorne, AM, 1990, The Northern Margin of the Capricorn Orogen, Western Australia — an example of an Early Proterozoic Collision Zone: Journal of Structural Geology, v. 12(5–6), p. 685–701.

Unsworth, MJ, Jones, AG, Wei, W, Marquis, G, Gokarn, SG, Spratt, SE, and the INDEPTH team, 2005, Crustal rheology of the Himalaya and Southern Tibet inferred from magnetotelluric data: Nature, v. 438(7064), p. 78–81.

Unsworth, MJ, Malin, PE, Egbert, GD, and Booker, JR, 1997, Internal structure of the San Andreas fault at Parkfield, California: Geology, v. 25(4), p. 359–362.

Vozoff, K, 1991, The magnetotelluric method, *in* Electromagnetic methods in applied geophysics — Applications Part A and Part B *edited by* MN Nabighian: Society of Exploration Geophysicists, p. 641–713.

Wannamaker, PE, Jiracek, GR, Stodt, JA, Caldwell, TA, Gonzalez, VM, McKnight, JD, and Porter, AD, 1989, Resistivity Cross-Section through the Defuca,Juan Subduction System and Its Tectonic Implications: Journal of Geophysical Research-Solid Earth and Planets, v. 94(B10), p. 14127–14144.

Wannamaker, PE, Hohmann, GW, and Ward, SH, 1984, Magnetotelluric Responses of 3-Dimensional Bodies in Layered Earths: Geophysics, v. 49(9), p. 1517–1533.

Wannamaker, PE, et al., 2002, Fluid generation and pathways beneath an active compressional orogen, the New Zealand Southern Alps, inferred from magnetotelluric data; Journal of Geophysical Research-Solid Earth, v. 107(B), 2117, doi: 1029/2001/JB000186.

Wiedelt, P, 1972, The inverse problem of geomagnetic induction. Z: Geophys., v. 38, p. 257–289.

Wiese, H, 1962, Geomagnetische tiefensondierung: Teil II; Die Streichrichtung der Untergrundstrikturen des elektrischen Widerstandes, erschlossen aus geomagnetischen variationen: Geofis. Pura et Appl., v. 52, p. 83–103.

Williams, SJ, 1986, Geology of the Gascoyne Province, Western Australia: Geological Survey of Western Australia, Report 15, 98p.

Wingate, MTD, and Giddings, JW, 2000, Age and palaeomagnetism of the Mundine Well dyke swarm, Western Australia: implications for an Australia-Laurentia connection at 755 Ma: Precambrian Research, v. 100(1–3), p. 335–357.

SELWAY

Magnetotelluric investigation into the electrical structure of the Capricorn Orogen, Western Australia

RECORD 2007/16

This Record is published in digital format (PDF) and is available online at: www.doir.wa.gov.au/GSWA/publications. Laser-printed copies can be ordered from the Information Centre for the cost of printing and binding.

Further details of geological publications and maps produced by the Geological Survey of Western Australia can be obtained by contacting:

Information Centre
Department of Industry and Resources
100 Plain Street
East Perth WA 6004
Phone: (08) 9222 3459 Fax: (08) 9222 3444

www.doir.wa.gov.au/GSWA/publications